



<b>Publication Year</b>	2020
<b>Acceptance in OA @INAF</b>	2021-09-01T10:39:20Z
<b>Title</b>	No Redshift Evolution in the Broad-line-region Metallicity up to $z = 7.54$ : Deep Near-infrared Spectroscopy of ULAS J1342+0928
<b>Authors</b>	Onoue, Masafusa; Bañados, Eduardo; Mazzucchelli, Chiara; Venemans, Bram P.; Schindler, Jan-Torge; et al.
<b>DOI</b>	10.3847/1538-4357/aba193
<b>Handle</b>	<a href="http://hdl.handle.net/20.500.12386/31005">http://hdl.handle.net/20.500.12386/31005</a>
<b>Journal</b>	THE ASTROPHYSICAL JOURNAL
<b>Number</b>	898



# No Redshift Evolution in the Broad-line-region Metallicity up to $z = 7.54$ : Deep Near-infrared Spectroscopy of ULAS J1342+0928

Masafusa Onoue<sup>1</sup>, Eduardo Bañados<sup>1</sup>, Chiara Mazzucchelli<sup>2</sup>, Bram P. Venemans<sup>1</sup>, Jan-Torge Schindler<sup>1</sup>, Fabian Walter<sup>1</sup>, Joseph F. Hennawi<sup>3</sup>, Irham Taufik Andika<sup>1</sup>, Frederick B. Davies<sup>4</sup>, Roberto Decarli<sup>5</sup>, Emanuele P. Farina<sup>1,6</sup>, Knud Jahnke<sup>1</sup>, Tohru Nagao<sup>7</sup>, Nozomu Tominaga<sup>8,9</sup>, and Feige Wang<sup>10,11,12</sup>

<sup>1</sup>Max-Planck-Institut für Astronomie, Königstuhl 17, D-69117 Heidelberg, Germany; [onoue@mpia-hd.mpg.de](mailto:onoue@mpia-hd.mpg.de)

<sup>2</sup>European Southern Observatory, Alonso de Córdova 3107, Vitacura, Región Metropolitana, Chile

<sup>3</sup>Department of Physics, Broida Hall, University of California at Santa Barbara, Santa Barbara, CA 93106, USA

<sup>4</sup>Lawrence Berkeley National Laboratory, 1 Cyclotron Rd., Berkeley, CA 94720, USA

<sup>5</sup>INAF-Osservatorio di Astrofisica e Scienza dello Spazio di Bologna, via Gobetti 93/3, I-40129, Bologna, Italy

<sup>6</sup>Max-Planck-Institut für Astrophysik, Karl-Schwarzschild-Straße 1, D-85748, Garching bei München, Germany

<sup>7</sup>Research Center for Space and Cosmic Evolution, Ehime University, Matsuyama, Ehime 790-8577, Japan

<sup>8</sup>Department of Physics, Faculty of Science and Engineering, Konan University, 8-9-1 Okamoto, Kobe, Hyogo 658-8501, Japan

<sup>9</sup>Kavli Institute for the Physics and Mathematics of the Universe (Kavli IPMU, WPI), The University of Tokyo, 5-1-5 Kashiwanoha, Kashiwa, Chiba 277-8583, Japan

<sup>10</sup>Steward Observatory, University of Arizona, 933 North Cherry Avenue, Tucson, AZ 85721, USA

<sup>11</sup>Department of Physics, University of California, Santa Barbara, CA 93106-9530, USA

Received 2020 January 20; revised 2020 June 6; accepted 2020 June 29; published 2020 July 29

## Abstract

We present deep (9 hr) Gemini-N/Gemini Near-InfraRed Spectrograph near-infrared spectroscopic observations of ULAS J1342+0928, a luminous quasar at  $z = 7.54$ . Various broad emission lines were detected, as well as the underlying continuum and iron forests over the rest-frame wavelength 970–2930 Å. There is a clear trend that higher-ionization emission lines show larger blueshifts with C IV  $\lambda 1549$  exhibiting  $5510_{-110}^{+240}$  km s<sup>-1</sup> blueshift with respect to the systematic redshift from the far-infrared [C II] 158  $\mu$ m emission line. Those high-ionization lines have wide profiles with FWHM more than 10,000 km s<sup>-1</sup>. A modest blueshift of  $340_{-80}^{+110}$  km s<sup>-1</sup> is also seen in Mg II, the lowest-ionization line identified in the spectrum. The updated Mg II-based black hole mass of  $M_{\text{BH}} = 9.1_{-1.3}^{+1.4} \times 10^8 M_{\odot}$  and the Eddington ratio of  $L_{\text{bol}}/L_{\text{Edd}} = 1.1_{-0.2}^{+0.2}$  confirm that ULAS J1342+0928 is powered by a massive and actively accreting black hole. There is no significant difference in the emission-line ratios such as Si IV/C IV and Al III/C IV when compared to lower-redshift quasars in a similar luminosity range, which suggests early metal pollution of the broad-line-region clouds. This trend also holds for the Fe II/Mg II line ratio, known as a cosmic clock that traces the iron enrichment in the early universe. Different iron templates and continuum fitting ranges were used to explore how the Fe II/Mg II measurement changes as a function of spectral modeling. Quasars at even higher redshift or at fainter luminosity range ( $L_{\text{bol}} \lesssim 10^{46}$  erg s<sup>-1</sup>) are needed to probe the sites of early metal enrichment and a corresponding change in the Fe II/Mg II ratio.

*Unified Astronomy Thesaurus concepts:* [Supermassive black holes \(1663\)](#); [Quasars \(1319\)](#)

## 1. Introduction

Quasars are among the most luminous objects in the universe. Powered by mass accretion onto the central supermassive black holes (SMBHs), quasars can be observed out to the epoch of cosmic reionization (at redshift  $z \gtrsim 6$ ), in which ultraviolet (UV) photons from the first-generation objects light up the dark universe (e.g., Fan et al. 2006; Planck Collaboration et al. 2016). Observations have reached this crucial epoch, e.g., by finding more than 200 quasars at  $z > 5.7$  (e.g., Fan et al. 2001; Willott et al. 2010; Venemans et al. 2013; Reed et al. 2015; Bañados et al. 2016; Jiang et al. 2016; Matsuoka et al. 2016; Wang et al. 2018). Six quasars have been identified at  $z > 7.0$  to date (Mortlock et al. 2011; Bañados et al. 2018; Wang et al. 2018; Matsuoka et al. 2019a, 2019b; Yang et al. 2019). A surprising fact drawn from those luminous quasars is that SMBHs are in place with  $M_{\text{BH}} \sim 10^9\text{--}10^{10} M_{\odot}$  in the early universe, which are as massive as the most massive SMBHs known in the entire cosmic history (e.g., Wu et al. 2015). This puts a stringent constraint on the formation scenario of SMBHs. The possible pathways to form such

gigantic SMBHs at  $z \gtrsim 6$  are through remnant BHs of Population III stars experiencing super-Eddington phases during their initial growth, formation of gigantic seed BHs ( $10^5\text{--}6 M_{\odot}$ ) through direct collapses of chemically pristine gas clouds, or runaway stellar collisions within dense metal-poor clusters, which leave  $10^3\text{--}4 M_{\odot}$  seed BHs (e.g., Greene et al. 2020; Inayoshi et al. 2020).

Chemical enrichment is another independent diagnostic to explore the early universe with high-redshift quasars (Hamann & Ferland 1999; Maiolino & Mannucci 2019). Unobscured quasars generally show broad emission lines in their rest-frame UV spectra with their typical line widths of several  $\times 10^3$  km s<sup>-1</sup>. These lines originate from the broad-line-region (BLR) gas, which orbits the central BHs at subparsec scale (e.g., Gravity Collaboration et al. 2018). The BLR gas-phase metallicity can be inferred from the observed emission-line ratios through photoionization modeling. Commonly used line combinations that are most sensitive to the BLR metallicity are, for example, NV  $\lambda 1240$ /He II  $\lambda 1640$  and NV  $\lambda 1240$ /C IV  $\lambda 1549$ . The BLR metallicity is thought to represent gas that was subject to the star formation history of the host galaxies, making quasars unique probes of the chemical enrichment.

<sup>12</sup> NHFP Hubble Fellow.

Although quasar surveys now probe the first billion years of the universe, there has been no clear evidence of redshift evolution in the BLR metallicity up to  $z \sim 7$ . The BLR clouds generally show supersolar metallicity ( $Z \sim 5Z_{\odot}$ ; e.g., Hamann & Ferland 1992, 1993; Dietrich et al. 2003b; Nagao et al. 2006b). Nagao et al. (2006b) show composite spectra of  $2.0 \leq z \leq 4.5$  quasars, showing almost constant BLR line ratios at fixed luminosity over the wide redshift range. Similar measurements have also been done for  $z \gtrsim 6$  quasars (e.g., Jiang et al. 2007; Juarez et al. 2009; De Rosa et al. 2011, 2014; Mazzucchelli et al. 2017; Tang et al. 2019), only to find possibly ubiquitous emission-line properties of unobscured quasars. Those studies suggest a rapid and intense chemical enrichment at the centers of the host galaxies, where star formation is most active. Narrow-line regions (NLRs) spreading over host galaxy scale also trace the host metallicity. The NLR gas metallicity is less extreme than that of the BLR, yet still close to or above the solar value (Storchi Bergmann et al. 1990), with no significant redshift evolution up to  $z \sim 5$  (Nagao et al. 2006a; Matsuoka et al. 2009, 2011a).

Among various BLR emission lines, the line ratio of UV Fe II complexes and Mg II  $\lambda 2798$  is of particular interest, since this quantity serves as a “cosmic clock” (Hamann & Ferland 1993; Yoshii et al. 1998). Supernova (SN) nucleosynthesis predicts that iron enrichment is delayed from  $\alpha$ -element by  $\sim 1$  Gyr owing to the longer timescale of Type Ia SNe (SNe Ia) than that of core-collapse Type II SNe (SNe II) (e.g., Greggio & Renzini 1983; Matteucci & Greggio 1986). Attempts have been made to detect the delayed iron enrichment in the early universe using Fe II/Mg II, as the two ions have similar ionizing potentials and their wavelengths overlap with each other. However, no significant redshift evolution has been identified yet up to  $z \sim 7$ , albeit the uncertainties are large in many cases (e.g., Kawara et al. 1996; Yoshii et al. 1998; Thompson et al. 1999; Dietrich et al. 2002a, 2003a; Iwamuro et al. 2002, 2004; Barth et al. 2003; Freudling et al. 2003; Maiolino et al. 2003; Jiang et al. 2007; Kurk et al. 2007; De Rosa et al. 2011, 2014; Mazzucchelli et al. 2017; Shin et al. 2019).

This paper shows our measurements of rest-frame UV BLR emission lines of a  $z = 7.54$  quasar, ULAS J1342+0928 (Bañados et al. 2018), using a deep near-IR (NIR) spectrum (9 hr on source) taken with the Gemini Near-Infrared Spectrograph (GNIRS) at the Gemini North telescope. From the first NIR data set obtained with Gemini/GNIRS and Folded-port InfraRed Echellette (FIRE) at the Magellan Baade telescope, ULAS J1342+0928 exhibits broad emission lines such as Ly $\alpha$ , C III], C IV, and Mg II (Bañados et al. 2018). From a simple modeling of quasar continuum and the Mg II line profile, the Mg II-based virial BH mass was estimated to be<sup>13</sup>  $M_{\text{BH}} = 7.6_{-1.9}^{+3.2} \times 10^8 M_{\odot}$  with its Eddington ratio of  $L_{\text{bol}}/L_{\text{Edd}} = 1.5_{-0.4}^{+0.5}$ . The main aim of this paper is a detailed spectral modeling of ULAS J1342+0928, in which the iron pseudo-continuum that spreads over  $\lambda_{\text{rest}} \approx 2000\text{--}3000 \text{ \AA}$  is taken into account. The structure of this paper is as follows: Our observations and data reduction are described in Section 2. The spectral analysis of the obtained NIR spectrum is presented in Section 3. The continuum and emission-line properties, as well as the measurements of line flux ratios and SMBH mass, are presented in Section 4. The systematic uncertainties

associated with the Mg II and Fe II measurements and the origin of early chemical enrichment in the early universe are discussed in Section 5. The summary and future prospects are given in Section 6.

Throughout this paper, the magnitudes quoted are in the AB system. We adopt a standard  $\Lambda$ CDM cosmology with  $H_0 = 70 \text{ km s}^{-1} \text{ Mpc}^{-1}$ ,  $\Omega_m = 0.3$ , and  $\Omega_{\Lambda} = 0.7$ . The [C II] 158  $\mu\text{m}$  redshift presented in Bañados et al. (2019;  $z_{[\text{CII}]} = 7.5400 \pm 0.0003$ ) is used as the systemic redshift of ULAS J1342+0928. The age of the universe was 680 Myr at this redshift in the chosen cosmology.

## 2. Data

### 2.1. Gemini/GNIRS Spectroscopy

The spectrum presented in this paper was taken in two different Gemini/GNIRS observation runs. The first run was on 2017 March 31 and April 3 with a 4.7 hr integration (GN-2017A-DD-4; PI: E.Bañados). The data were presented in Bañados et al. (2018). The second observing run was executed between 2019 May 27 and June 2 (GN-2019A-FT-115; PI: M. Onoue), with a 4.3 hr integration. In this paper, both GNIRS data sets of ULAS J1342+0928 were combined, which results in a total integration time of 9.0 hr.

Both runs were executed with the same setup. With the 31.7 line  $\text{mm}^{-1}$  grating and the short camera ( $0''.15 \text{ pixel}^{-1}$ ), the cross-dispersed mode was used to cover the observed wavelengths of  $\lambda_{\text{obs}} \sim 0.9\text{--}2.5 \mu\text{m}$ , which corresponds to the rest-frame wavelengths of  $\lambda_{\text{rest}} = 970\text{--}2930 \text{ \AA}$ . The slit width was chosen to be  $0''.675$  to perform our spectroscopy with a spectral resolution of  $R \sim 760$ . The single exposure time was set to 300 s with the standard ABBA nodding offsets between exposures. The observation was carried out in good weather conditions with the seeing size of  $\sim 0''.4\text{--}0''.9$  and at air mass  $\sim 1.1\text{--}1.5$  (with a few exposures at  $< 1.8$ ).

### 2.2. Data Reduction

Data reduction was performed with PyPeIt, an open-source spectroscopic data reduction pipeline developed by Prochaska et al. (2020). Since the target was observed on six different dates, the raw data taken on the same date were processed with the pipeline to obtain calibrated one-dimensional (1D) spectra. Each exposure was bias-subtracted and flat-fielded using standard procedures. The wavelength solution was obtained by comparing the spectrum of the sky with the prominent OH (Rousselot et al. 2000) and water lines.<sup>14</sup> After removing contamination from cosmic ray using the algorithm of van Dokkum (2001), the pipeline optimally subtracts the background by modeling the sky emission with a b-spline function that follows the curvature of the spectrum on the detector (Kelson 2003). The 1D spectrum of the quasar was extracted for each exposure using optimal weighting.

The individual 1D spectra were flux-calibrated by fitting for the the order-by-order sensitivity function derived from the A-type stars observed before or after the target exposures. The initially fluxed 1D spectra from each night were then co-added across the orders to compute a single co-added and fluxed spectrum, but with the telluric absorption still present. Then, a telluric model was directly fitted to the co-added quasar spectrum using the telluric model grids produced from the

<sup>13</sup> The given SMBH mass and Eddington ratio reported in Bañados et al. (2018) are modified to the cosmology in this paper, because Bañados et al. (2018) use the Planck cosmology with  $H_0 = 67.7 \text{ km s}^{-1} \text{ Mpc}^{-1}$ ,  $\Omega_m = 0.307$ , and  $\Omega_{\Lambda} = 0.693$  (Planck Collaboration et al. 2016).

<sup>14</sup> <https://hitran.org/>

Line-By-Line Radiative Transfer Model (LBLRTM<sup>15</sup>; Clough et al. 2005). Specifically, a principal component analysis (PCA) model of the quasar continuum was constructed spanning from 1216 to 3100 Å in the quasar rest frame following the procedure described in Davies et al. (2018). This models the quasar as a linear combination of a mean quasar spectrum and seven PCA components. A joint fit was performed for the telluric absorption and PCA continuum to obtain the seven PCA coefficients and overall normalization of the spectrum, as well as the resolution, an overall spectral shift, and four parameters describing the atmosphere (air mass, pressure, temperature, and water vapor).

Those six initially co-added spectra were then resampled in the velocity space by measuring the inverse-square weighted average at 200 km s<sup>-1</sup> bins. Absolute flux calibration was performed by scaling the spectra to the *J*-band photometry reported in Bañados et al. (2018,  $J = 20.30 \pm 0.02$ ). This procedure effectively corrects for any slit loss. Finally, all six fluxed and telluric-corrected 1D spectra were co-added to obtain the final spectrum. Figure 1 shows this final GNIRS spectrum in rest frame, in which the atmospheric transmission curve as a function of the observed wavelength is also shown.

### 3. Spectral Analysis

A multicomponent (continuum+iron+emission lines) fit was applied to the GNIRS spectrum of ULAS J1342+0928. Three components were considered to decompose the observed continuum: power-law continuum ( $F_{\lambda}^{\text{PL}}$ ), Balmer continuum ( $F_{\lambda}^{\text{BC}}$ ), and iron pseudocontinuum ( $F_{\lambda}^{\text{Fe II+Fe III}}$ ). The free parameters are the scale factor and slope of the power-law continuum and the scale factor of iron pseudocontinuum. The Balmer continuum is tied to the power-law continuum with a fixed relative scale, as described in detail below.

#### 3.1. Continuum

The quasar continuum needs to be subtracted from the spectrum to measure the profiles of broad emission lines. A sum of two continuum components was considered: power-law continuum ( $F_{\lambda}^{\text{PL}} = F_0 \lambda^{\alpha_{\lambda}}$ ) and the Balmer continuum. For the latter, Grandi (1982) introduced the following formula:

$$F_{\lambda}^{\text{BC}} = F_0^{\text{BE}} B_{\lambda}(T_e) (1 - \exp(-\tau_{\text{BE}}(\lambda/\lambda_{\text{BE}})^3)), \quad (1)$$

where  $B_{\lambda}(T_e)$  is the Planck function at electron temperature  $T_e$ , and  $\tau_{\text{BE}}$  is optical depth at the Balmer edge  $\lambda_{\text{BE}}$  ( $=3646$  Å). The strength of the Balmer continuum flux cannot be well constrained for the obtained spectrum owing to the limited wavelength coverage and the degeneracy with the power-law and iron components. In this study, the normalization factor  $F_0^{\text{BE}}$  was fixed to be 30% of the power-law continuum at  $\lambda_{\text{rest}} = 3675$  Å. The two parameters,  $T_e$  and  $\tau_{\text{BE}}$ , were fixed to be  $T_e = 15,000$  K and  $\tau_{\text{BE}} = 1$ , respectively. Those assumptions were also made in the literature (Dietrich et al. 2003a; Kurk et al. 2007; De Rosa et al. 2011; Mazzucchelli et al. 2017; Shin et al. 2019).

Different normalizations of the Balmer continuum were also tested from 0% to 100% of the power-law continuum at  $\lambda_{\text{rest}} = 3675$  Å in order to address the validity of our assumption and the potential systematic uncertainties on the Fe II and Mg II

flux measurements. As a result, the normalization factor of  $\sim 0$ –30% gave reasonable spectral decomposition with little changes in the Fe II/Mg II flux ratios (within the  $1\sigma$  uncertainty of our fiducial value). Therefore, our assumption of the normalization factor is robust to the extent of giving accurate flux measurements of Fe II and Mg II. More details are described in Section 5.1.

#### 3.2. Iron Emission Lines

Two empirical templates were used to fit the UV iron (Fe II + Fe III) pseudocontinuum for comparison. For the UV Fe II measurements, one of the most frequently used iron templates for the UV Fe II flux measurements is from Vestergaard & Wilkes (2001, hereafter **VW01** template), while another template from Tsuzuki et al. (2006, hereafter **T06** template) has also been used recently (e.g., Sameshima et al. 2017; Woo et al. 2018; Shin et al. 2019). Both templates are from a high-resolution spectrum of I Zw 1, a narrow-line Seyfert 1 galaxy at  $z = 0.061$ , which exhibits narrow and strong iron emission lines. The main difference between these two templates is their behavior around the Mg II line. The **T06** template takes into account the Fe II contribution underneath the Mg II line, using their model spectrum based on a photoionization calculation of the BLR clouds. On the other hand, the **VW01** template has no Fe II flux in this region, which in turn overestimates the actual Mg II flux in the line fitting. For this reason, the **T06** template was selected as our primary template to accurately measure the Fe II and Mg II fluxes. The **T06** template was augmented with the **VW01** template at  $\lambda_{\text{rest}} \leq 2200$  Å. Following an empirical correction for the oversubtracted Fe II flux of the **VW01** template, constant flux was added to the **VW01** template at  $\lambda_{\text{rest}} = 2770$ –2820 Å, the amount of which is 20% of the mean flux at  $\lambda_{\text{rest}} = 2930$ –2970 Å (Kurk et al. 2007). Still, the modified **VW01** iron template gives a smaller Fe II/Mg II flux ratio of ULAS J1342+0928 than that measured with the **T06** template. This issue is revisited in Section 5.1.

The iron templates were then convolved with Gaussian kernels to generate a wide range of velocity dispersion of FWHM = 500–10,000 km s<sup>-1</sup>, with a step of 500 km s<sup>-1</sup>. Finally, those templates were redshifted to the systemic redshift of ULAS J1342+0928. A potential velocity shift of the iron emission lines is not considered in this study.

#### 3.3. Continuum and Iron Fitting Procedure

The power-law plus Balmer continuum model and the iron templates were iteratively fitted to the observed spectrum. In this study, the following wavelength ranges were selected as continuum windows:  $\lambda_{\text{rest}} = 1275$ –1285 Å, 1310–1325 Å, 2500–2750 Å, and 2850–2890 Å. The first two were chosen to be line-free regions around the O I + Si II line at  $\lambda_{\text{rest}} = 1305$  Å. The latter two ranges were also used for fitting the iron templates. The iron fluxes at those two wavelength ranges are dominated by Fe II (Vestergaard & Wilkes 2001). The UV Fe II bump actually exists over a wider wavelength region of  $\lambda_{\text{rest}} \approx 2200$ –3000 Å, but weak noniron emission lines also exist at  $2200$  Å  $< \lambda_{\text{rest}} < 2500$  Å, such as C II  $\lambda 2326$ , Fe III UV 47 at  $\lambda_{\text{rest}} \approx 2418$  Å (not covered by the iron templates), and [O II]  $\lambda 2470$ .

Other wavelength ranges such as  $\lambda_{\text{rest}} = 1425$ –1470 Å, 1680–1710 Å, and 1975–2050 Å were also used in the literature for continuum fitting; however, those were excluded

<sup>15</sup> <http://rtweb.aer.com/lblrtm.html>

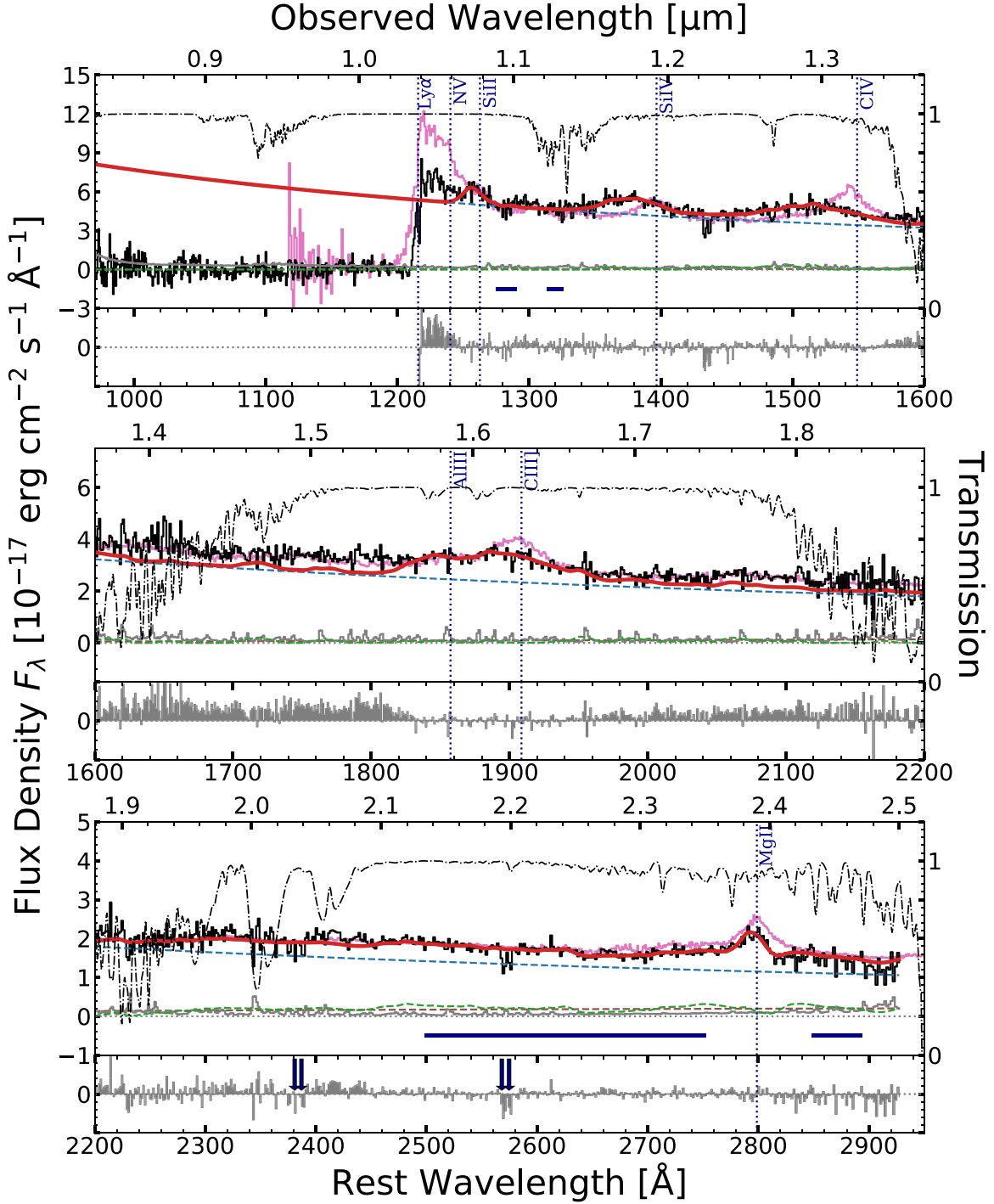


**Figure 1.** Gemini/GNIRS spectrum of ULAS J1342+0928 at  $\lambda_{\text{rest}} = 970\text{--}2930 \text{ \AA}$  (black) with its error spectrum (gray). The spectrum is shifted to rest frame with the [C II] redshift measured in Bañados et al. (2019). Both the rest frame and the observed wavelength are indicated at the bottom and top of each panel, respectively. The dashed lines show the best-fit decomposition of power-law continuum (blue), Balmer continuum (brown), and the scaled iron template from Tsuzuki et al. (2006, green). The red line shows the sum of those three components and emission lines fitted with single Gaussian profiles. In each of the three wavelength regions, the residual flux is shown in the bottom subpanel. The composite spectrum of  $z \sim 6$  quasars from Shen et al. (2019) is overplotted (magenta), normalized by the  $J$ -,  $H$ -, and  $K_s$ -band magnitudes reported in Bañados et al. (2018) from the top to bottom panels. The wavelength ranges used for continuum fitting are indicated with solid blue lines. The iron templates were fitted in the reddest two windows. The black dotted-dashed line shows the atmospheric transmission curve obtained for the spectrum taken on one of the observing dates (2017 April 3). Two  $z > 6$  Mg II doublet absorbers reported in Cooper et al. (2019) are indicated with arrows.

for our spectral fitting of ULAS J1342+0928 for the following reasons. First, ULAS J1342+0928 has extremely broad emission lines with FWHM more than  $10,000 \text{ km s}^{-1}$ , and therefore the broad outskirts of the emission lines contribute to the observed flux between Si IV and C IV, and also at the redder

side of C III]. Second, weak emission lines are present and heavily blended between C IV and C III]: He II  $\lambda 1640$ , O III]  $\lambda 1663$ , N IV  $\lambda 1719$ , Al II  $\lambda 1722$ , N III]  $\lambda 1750$ , and Fe II (Vanden Berk et al. 2001; Nagao et al. 2006b). In these wavelength regions, the observed flux deviates from the

**Table 1**  
Continuum Properties of ULAS J1342+0928

$\alpha_\lambda$	$F_0$ ( $10^{-10}$ erg cm $^{-2}$ s $^{-1}$ Å $^{-1}$ )	$M_{1450}$ (mag)	$\lambda L_{3000}$ ( $10^{46}$ erg s $^{-1}$ )	$L_{\text{bol}}$ ( $10^{47}$ erg s $^{-1}$ )
$-1.84_{-0.01}^{+0.03}$	$1.60_{-0.37}^{+0.13}$	$-26.57 \pm 0.04$	$2.47 \pm 0.03$	$1.27 \pm 0.02$

**Note.** Those continuum properties are based on the best-fit power-law component of the **T06** model. The continuum luminosity for the **VW01** iron model is identical to the **T06** model.

intrinsic power-law continuum as a result of those weak lines. Also, the iron templates include Fe III forest at  $\lambda_{\text{rest}} = 1900\text{--}2100$  Å. This region should be excluded from the continuum and iron windows, as the Fe II line flux is our primary interest. The continuum flux is overestimated if those wavelength regions are used in the continuum+iron fitting, which ends up underestimating the Fe II flux.

To derive the continuum and iron template parameters, an initial continuum model was fitted to the spectrum, after which the iron templates were fitted to the continuum-subtracted residuals. The continuum model was then refitted to the spectrum after subtracting the iron contribution from the original spectrum. The same continuum and iron template fittings were repeated until the iron template fitting achieves a convergence of  $<1\%$ . The continuum+iron models were fitted by all the iron templates with different line broadening. The model that gave the minimum chi-square at the iron windows was adopted as the best model.

Another iterative fitting was done to test potential over-subtraction of the continuum, in which the initial continuum scale was set to 10% of the value derived in the continuum-only fitting. Even in this case, the scales of continuum and the **T06** iron template converged at the values that are in agreement with the originally determined ones within 1%. There was no change in the selected widths of Fe II+Fe III.

The best-fit continuum parameters for the **T06** model are reported in Table 1. Those continuum parameters agree with the **VW01** model within  $1\sigma$  uncertainty. The absolute magnitude at rest frame 1450 Å and monochromatic luminosity at rest frame 3000 Å ( $\lambda L_{3000}$ ) were measured from the sum of the fluxes of the best-fit power-law and Balmer continuum models. The bolometric luminosity  $L_{\text{bol}}$  was derived by applying a bolometric correction of  $L_{\text{bol}} = 5.15 \times \lambda L_{3000}$  (Richards et al. 2006). For the Fe II flux, the scaled iron templates were integrated over  $2200 \text{ \AA} \leq \lambda_{\text{rest}} \leq 3090 \text{ \AA}$ . The integrated Fe II flux was divided by the continuum flux at  $\lambda_{\text{rest}} = 3000 \text{ \AA}$  to derive the equivalent width. This procedure allows for direct comparison with the low-redshift quasars presented in Sameshima et al. (2017), as they derived the Fe II equivalent widths in the same way.

There are metal absorption lines imprinted on the quasar spectrum. A detailed analysis of those metal absorbers will be presented elsewhere, and only the  $z > 6$  Mg II absorbers reported in Cooper et al. (2019)<sup>16</sup> are shown in Figure 1. Those metal absorption lines were automatically masked in the continuum fitting by clipping regions where the observed flux deviates from the best-fit continuum plus emission-line model by more than  $3\sigma$  of the flux error at each pixel.

### 3.4. Emission Lines

After subtracting the best-fit continuum (power-law and Balmer continuum) and scaled iron templates, broad emission

lines were simultaneously fitted with single Gaussian profiles, from which line widths, equivalent widths, and velocity blueshifts from the [C II] redshift were measured for each line. The emission lines considered in this paper (except Fe II and Fe III) are Ly $\alpha$ +N V  $\lambda$ 1240, Si II  $\lambda$ 1263, Si IV  $\lambda$ 1397, C IV  $\lambda$ 1549, Al III  $\lambda$ 1857, C III]  $\lambda$ 1909, and Mg II  $\lambda$ 2798.

In some cases, those emission lines have neighboring weak lines, specifically Si IV+O IV]  $\lambda$ 1397, 1402 and Si III] +C III]  $\lambda$ 1892, 1909. Since those lines could not be deblended owing to their extremely broad nature and the modest spectral resolution, single Gaussians were fitted to those two multiplets for simplicity. For C III], the UV Fe III emission lines at  $\lambda_{\text{rest}} \approx 1900$  Å may also contaminate to the C III] flux, as Fe III was not directly fitted to the spectrum but just scaled by the same factor of Fe II determined at  $\lambda_{\text{rest}} > 2200$  Å. Al III  $\lambda$ 1857 and C III]  $\lambda$ 1909 were simultaneously fitted with two Gaussian profiles. The two lines were fitted at  $\lambda_{\text{rest}} = 1827\text{--}1914$  Å to avoid contamination from adjacent weak lines. Also, C IV was fitted at  $\lambda_{\text{rest}} \leq 1570$  Å not to be contaminated by the unidentified He II  $\lambda$ 1640.

N V  $\lambda$ 1240 is heavily blended with Ly $\alpha$  and could not be identified as a single line. For this reason, the line flux of the Ly $\alpha$ +N V composite was measured instead by summing the flux above the power-law continuum at  $\lambda_{\text{rest}} = 1160\text{--}1290$  Å (Diamond-Stanic et al. 2009). Note that the flux measured with this procedure includes Si II, which was individually fitted with a single Gaussian profile in this study. Nevertheless, the same definition of the Ly $\alpha$ +N V equivalent width was taken for consistency with the literature.

The uncertainties of the continuum and emission-line properties were measured with a Monte Carlo simulation, in which 1000 mock spectra were generated by adding random noise to the observed spectrum using the flux errors. Both the continuum and emission-line parameters were repeatedly measured for each realization, to take into account the effects of continuum errors on the emission-line measurements. The  $1\sigma$  uncertainty range for each quantity was then measured by the 16th and 84th percentiles. Table 2 shows the emission-line profiles of ULAS J1342+0928 for the **T06** model, while the Mg II and Fe II profiles for the **VW01** model are also shown in the same table.

## 4. Results

Here, the results of the UV spectral modeling of ULAS J1342+0928 are presented based on the **T06** model, unless otherwise stated.

### 4.1. Continuum Properties

The continuum slope of  $\alpha_\lambda = -1.84_{-0.01}^{+0.03}$  is a typical value for lower-redshift quasars (e.g., Vanden Berk et al. 2001; Selsing et al. 2016). In Bañados et al. (2018), only the power-law component was considered for their continuum model. The derived absolute magnitude at rest frame 1450 Å in our new

<sup>16</sup> Those absorbers were identified with their FIRE spectrum, which has a higher spectral resolution than the GNIRS spectrum presented in this paper.

**Table 2**  
Emission-line Properties of ULAS J1342+0928

	Ly $\alpha$ +N V <sup>a</sup>	Si II	Si IV	C IV	Al III	C III]	Mg II	Fe II	Mg II <sub>VW01</sub>	Fe II <sub>VW01</sub>
FWHM (km s <sup>-1</sup> )	...	4040 <sup>+300</sup> <sub>-290</sub>	10840 <sup>+350</sup> <sub>-380</sub>	16000 <sup>+390</sup> <sub>-430</sub>	5300 <sup>+610</sup> <sub>-670</sub>	11880 <sup>+470</sup> <sub>-630</sub>	2830 <sup>+210</sup> <sub>-210</sub>	1500	3780 <sup>+220</sup> <sub>-260</sub>	3500
EW <sub>rest</sub> (Å)	12.5 <sup>+1.3</sup> <sub>-0.2</sub>	4.3 <sup>+0.4</sup> <sub>-0.3</sub>	14.3 <sup>+0.8</sup> <sub>-0.8</sub>	23.2 <sup>+1.0</sup> <sub>-1.0</sub>	6.7 <sup>+1.2</sup> <sub>-1.0</sub>	31.9 <sup>+1.0</sup> <sub>-1.9</sub>	13.4 <sup>+0.8</sup> <sub>-0.9</sub>	126 <sup>+6</sup> <sub>-15</sub>	19.9 <sup>+0.7</sup> <sub>-1.5</sub>	123 <sup>+4</sup> <sub>-19</sub>
$\Delta v_{[C II]}$ (km s <sup>-1</sup> )	...	1340 <sup>+100</sup> <sub>-90</sub>	3640 <sup>+150</sup> <sub>-130</sub>	5510 <sup>+240</sup> <sub>-110</sub>	2630 <sup>+330</sup> <sub>-320</sub>	2020 <sup>+180</sup> <sub>-190</sub>	340 <sup>+110</sup> <sub>-80</sub>	...	750 <sup>+90</sup> <sub>-90</sub>	...

**Note.** The line measurements are based on the T06 model, while for Mg II and Fe II, those based on our VW01 model are also reported in the last two columns. For the other emission lines considered, the two models agree with each other within  $2\sigma$ . The line widths are corrected for instrumental broadening. The positive values in  $\Delta v_{[C II]}$  are blueshifts with respect to [C II].

<sup>a</sup> The Ly $\alpha$  + N V equivalent width includes the Si II  $\lambda$ 1263 contribution, as the line flux was measured by summing flux above the continuum models at  $\lambda_{rest} = 1160$ –1290 Å, following the empirical definition of Diamond-Stanic et al. (2009).

continuum fitting,  $M_{1450} = -26.57 \pm 0.04$ , is fainter than the previously reported value by  $\Delta M_{1450} = 0.19$  mag. This difference is mostly attributed to the contribution of iron emission lines, which is taken into account in this work, while the different cosmology used in Bañados et al. (2018,  $H_0 = 67.7 \text{ km s}^{-1} \text{ Mpc}^{-1}$ ,  $\Omega_m = 0.307$ ,  $\Omega_\Lambda = 0.693$ ) accounts for 0.06 mag of the difference compared to our new measurement.

#### 4.2. Broad Emission Line Properties

ULAS J1342+0928 is characterized by highly blueshifted and broad high-ionization lines. Figure 2 shows the line blueshifts for the broad emission lines detected in ULAS J1342+0928 as a function of ionization potentials. The amounts of blueshifts are proportional to the ionization potentials, with the high-ionization lines such as C IV (ionization potential: 47.9 eV) and Si IV (33.5 eV) showing more than 3000 km s<sup>-1</sup> blueshifts with respect to the [C II] redshift ( $\Delta v_{[C II]} = 5510_{-110}^{+240}$  km s<sup>-1</sup> and  $3640_{-130}^{+150}$  km s<sup>-1</sup>, respectively). The correlation between the ionization potentials and the blueshifts was reported in Vanden Berk et al. (2001), in which they showed a composite spectrum of  $z \approx 1$  quasars from the Sloan Digital Sky Survey (SDSS; York et al. 2000). The blueshifts of the SDSS  $z \approx 1$  quasars with respect to the forbidden [O III]  $\lambda$ 5007 line are much smaller than those found in ULAS J1342+0928 for the same lines ( $<560$  km s<sup>-1</sup>; see Figure 2).<sup>17</sup>

The blueshifts of ULAS J1342+0928 are even larger than those of quasars at similar redshifts. The composite spectrum of  $z \sim 6$  luminous quasars from Shen et al. (2019) is overplotted on the ULAS J1342+0928's spectrum in Figure 1, where it is evident that ULAS J1342+0928 has larger blueshifts than the average of  $z \sim 6$  quasars. Meyer et al. (2019) argue that, with their compilation of luminosity-matched  $1.5 \lesssim z \lesssim 7.5$  quasars including ULAS J1342+0928, the C IV blueshift sharply increases at  $z \gtrsim 6$ . In Meyer et al. (2019), there are 16 quasars for which the far-infrared (FIR) [C II] and/or CO (6–5) lines were detected in the literature (Carilli et al. 2007; Wang et al. 2013, 2016; Bañados et al. 2015; Venemans et al. 2016, 2017a, 2019; Mazzucchelli et al. 2017; Decarli et al. 2018). The average blueshifts with respect to the systemic redshifts from the rest–FIR emission lines,<sup>18</sup> as well as their standard deviation, are shown in Figure 2. For Mg II, C III], Si IV, and C IV, ULAS J1342

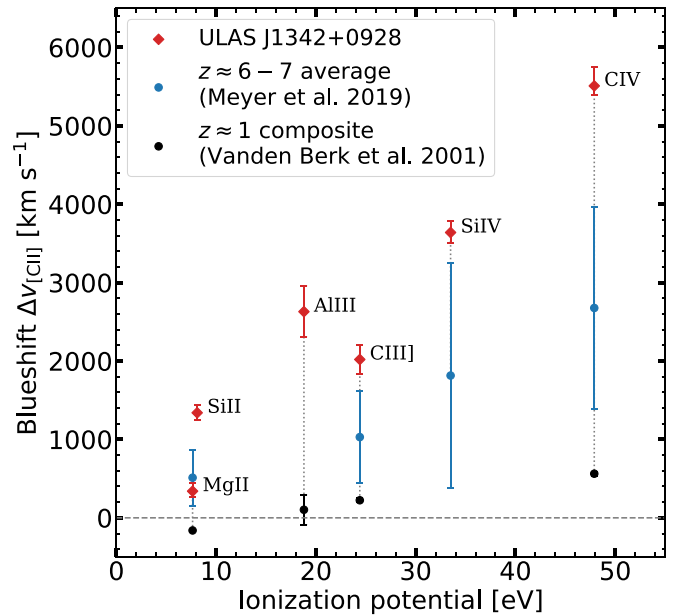


**Figure 2.** Emission-line blueshifts as a function of ionization potentials. Positive values are blueshifts. The blueshifts of ULAS J1342+0928 with respect to the [C II] 158  $\mu\text{m}$  line are shown with red diamonds, with the measurement errors indicated by the error bars. The average blueshifts of  $z \approx 6$ –7 quasars in Meyer et al. (2019), except their measurements for J1342+0928) are shown with blue circles, with the error bars showing the standard deviation. For these measurements, 16 quasars are used for which the rest–FIR [C II] or CO (6–5) redshifts are available in the literature (see text for details). The blueshifts in the composite spectrum of the low-redshift ( $z \approx 1$ ) SDSS quasars with respect to [O III]  $\lambda$ 5007 (Vanden Berk et al. 2001) are shown with black circles. Note that Si II and Si IV were identified in Vanden Berk et al. (2001) but were excluded in their blueshift measurements, because they took into consideration the line blending of Si II with Ly $\alpha$ +N V and of Si IV with [O IV].

+0928 has similar or higher blueshifts than this average by a factor of up to 2, indicating extreme outflowing components in the BLR clouds.

High-ionization emission lines are easily affected by the BLR outflow, showing  $\Delta v \approx 1000$ –2000 km s<sup>-1</sup> velocity shifts in general (e.g., Richards et al. 2011; Shen et al. 2016; Ge et al. 2019). Figure 3 compares the best-fit Gaussian profiles of those emission lines in the velocity space with the lines color-coded by the ionization potentials. There is a trend of wider widths in more largely blueshifted (or higher-ionization) emission lines up to FWHM = 16,000 km s<sup>-1</sup>, which is seen in C IV. This is perhaps a natural consequence of the highly blueshifted emission lines that likely have both virialized and outflowing components (Vietri et al. 2018), albeit the broad emission lines of ULAS J1342+0928 are well modeled with

<sup>17</sup> The narrow [O III]  $\lambda$ 5007 line is known to trace the systemic redshift well (with the typical blueshift of 40 km s<sup>-1</sup>), while in some cases (e.g., high Eddington ratios) this could show significant blueshifts up to 400 km s<sup>-1</sup> (e.g., Boroson 2005).

<sup>18</sup> [C II] redshift was prioritized when both the [C II] and CO (6–5) redshifts are available.

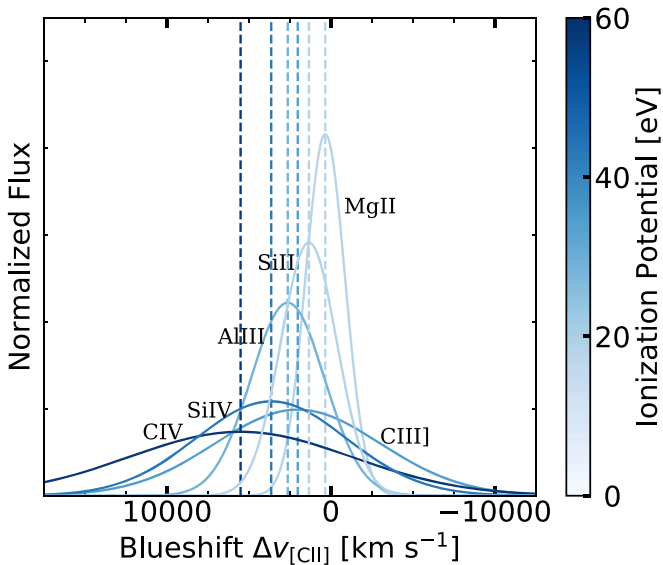


**Figure 3.** Comparison of the best-fit Gaussian profiles of the detected broad emission lines in the velocity space. The velocity zero-point is set to the systemic [C II] redshift from Bañados et al. (2019). The line strengths are scaled so that the integrated fluxes are the same. The line ionization potentials are indicated with the line colors (higher-ionization lines have darker colors). The line centers are indicated with dashed lines. As is also partly seen in Figure 2, there is a tendency that higher-ionization lines have larger blueshifts and wider profiles.

single Gaussian profiles. Vietri et al. (2018) found that the most luminous class of  $2 < z < 4$  quasars at  $L_{\text{bol}} > 2 \times 10^{47}$  erg  $\text{s}^{-1}$ , which is slightly brighter than ULAS J1342+0928, show similarly large blueshifts up to 8000  $\text{km s}^{-1}$ . ULAS J1342+0928 falls at a similar location to their samples in the C IV blueshift—equivalent width plane (Richards et al. 2011; Plotkin et al. 2015; Coatman et al. 2017).

It is also remarkable that Mg II, the lowest-ionization line among the detected emission lines with the ionization potential of 7.6 eV, has a modest blueshift of  $\Delta v_{\text{Mg II}-[\text{C II}]} = 340^{+110}_{-80}$   $\text{km s}^{-1}$ . A larger value was reported in Bañados et al. (2018,  $\Delta v_{\text{Mg II}-[\text{C II}]} = 500 \pm 140$   $\text{km s}^{-1}$ ), where only the power-law continuum was considered in the spectral modeling (see Section 3 for the details of our modeling in this paper). The same trend has also been reported in other luminous quasars at  $z \gtrsim 6$  (Venemans et al. 2016; Wang et al. 2016; Mazzucchelli et al. 2017). Venemans et al. (2016) showed similar Mg II blueshifts with respect to [C II] and/or CO (6–5) for their 11 quasars at  $z \gtrsim 6$  (their mean and standard deviation are  $\Delta v_{\text{Mg II}-[\text{C II}]/\text{CO}} = 480 \pm 630$   $\text{km s}^{-1}$ ).

The  $\text{Ly}\alpha + \text{N V}$  equivalent width  $\text{EW}(\text{Ly}\alpha + \text{N V})_{\text{rest}} = 12.5^{+1.3}_{-0.2}$  Å classifies ULAS J1342+0928 as a weak-line quasar according to an empirical definition of Diamond-Stanic et al. (2009,  $\text{EW}(\text{Ly}\alpha + \text{N V})_{\text{rest}} < 15.4$  Å), which is based on 3000 quasars at  $3 < z < 5$ . This value is also smaller than the mean property of  $z \sim 6$  quasars compiled in Bañados et al. (2016), which shows  $\langle \text{EW}(\text{Ly}\alpha + \text{N V})_{\text{rest}} \rangle \geq 34.7$  Å ( $1\sigma$  range of 14.2–85.7 Å) for their compilation of 117 quasars at  $z > 5.6$ . However, the weak-line nature of  $\text{Ly}\alpha + \text{N V}$  is likely due to strong absorption by the intergalactic medium (IGM) in the line of sight. The IGM neutral fraction at  $z > 7$  is so strong that the  $\text{Ly}\alpha$  damping wing suppresses the quasar emission even redward of  $\text{Ly}\alpha$  (Bañados et al. 2018; Davies et al. 2018). To support this argument, the C IV equivalent width of ULAS

J1342+0928,  $\text{EW}(\text{C IV})_{\text{rest}} = 23.2^{+1.0}_{-1.0}$  Å, is just close to the  $1\sigma$  range reported in Diamond-Stanic et al. (2009;  $1\sigma$  range: 26.1–67.4 Å), even though Shen et al. (2019) showed that the weak-line quasar fraction with  $\text{EW}(\text{C IV})_{\text{rest}} < 10$  Å increases toward  $z \sim 6$ . Therefore, it is likely that the weak  $\text{Ly}\alpha$  is not an intrinsic characteristic of ULAS J1342+0928, and the inherent strength of the BLR emission lines is similar to that of lower-redshift quasars.

### 4.3. Line Ratios

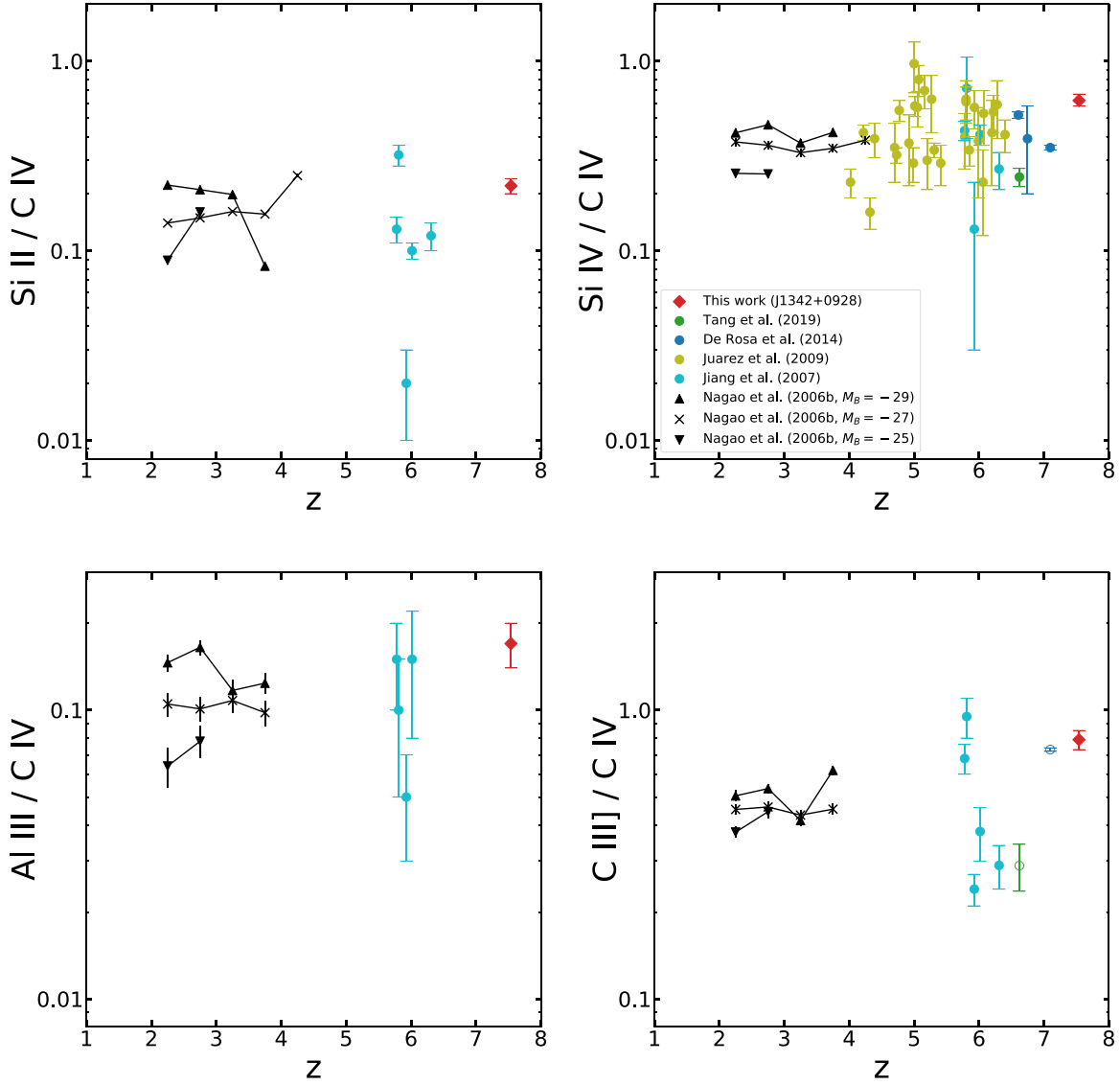
The flux ratios of the BLR emission lines are used to test whether ULAS J1342+0928 has a metal-poor BLR when the universe was 680 million years old. Table 3 shows the line ratios of Si II/C IV, Si IV/C IV, Al III/C IV, C III]/C IV, and Fe II/Mg II. Those line combinations (except Fe II/Mg II) are in fact second-order tracers of the BLR metallicity, while other line combinations such as N V/He II and N V/C IV were known as the better diagnostics (e.g., Hamann & Ferland 1993; Hamann et al. 2002; Dietrich et al. 2003b; Nagao et al. 2006b). However, neither N V nor He II was identified in ULAS J1342+0928 owing to their weakness, heavy line blending, and/or atmospheric absorption (Figure 1). Also, the red tail of the damping wing may suppress N V (Bañados et al. 2018; Davies et al. 2018).

Figure 4 shows the line ratios as a function of redshift. The lower-redshift data points come from the literature: Jiang et al. (2007), De Rosa et al. (2014), and Tang et al. (2019) for  $6 \lesssim z \lesssim 7$ , Juárez et al. (2009) for  $4 \lesssim z \lesssim 6$ , and Nagao et al. (2006b) for  $2 \lesssim z \lesssim 4$ . Since there is a magnitude dependence in the BLR line ratios, the subsets of the  $2 \lesssim z \lesssim 4$  measurements are shown with different  $B$ -band magnitude bins, namely,  $-29.5 \leq M_B \leq -28.5$ ,  $-27.5 \leq M_B \leq -26.5$ , and  $-25.5 \leq M_B \leq -24.5$ .

Those emission-line ratios have a positive correlation with the BLR metallicity. Therefore, our result suggests that J1342+0928 has a comparable BLR metallicity to the lower-redshift quasars. This result extends the no redshift evolution trend of the BLR metallicity up to  $z = 7.5$ . The magnitude dependence of the emission-line ratios does not affect our conclusion, because the  $4 \lesssim z \lesssim 7$  quasars shown in Figure 4 are primarily at the most luminous range ( $L_{\text{bol}} \gtrsim 10^{46}$  erg  $\text{s}^{-1}$ ).

It is important to recall that Si IV and C III] have adjacent weak lines (i.e., O IV]  $\lambda 1402$  and Si III]  $\lambda 1892$ ) that were ignored in the line fitting and were therefore not deblended. Specifically, O IV] may contribute to the observed Si IV/C IV line ratio, although the previous studies plotted in the top right panel of Figure 4 also modeled the blended Si IV+O IV] line as a single line. For Al III+Si III]+C III], Nagao et al. (2006b) were able to deblend the three lines, while De Rosa et al. (2014) and Tang et al. (2019) assumed the multiplet line as a single line. Jiang et al. (2016) deblended Al III and C III], and they ignored Si III] as did this study. In Figure 4, Al III/C IV line ratios are shown in the case in which Al III was measured as a single line. For C III], the sum of C III] and Si III] is shown for the measurements of Nagao et al. (2006b), to be consistent with Jiang et al. (2007) and this study. Although Al III was not deblended, the C III]/C IV measurements of De Rosa et al. (2014) and Tang et al. (2019) are also shown in Figure 4 for reference. In fact, the relative strength of Si III] with respect to C III] is controversial, and this third line could add significant flux around C III] (see Section 4.1; Nagao et al. 2006b). Moreover, there could be a nonnegligible contribution of the





**Figure 4.** Emission-line ratios as a function of redshift. The colors and symbols are the same in the four panels: red for J1342+0928 (T06 model), blue for De Rosa et al. (2014), green for Tang et al. (2019), cyan for Jiang et al. (2007), yellow for Juarez et al. (2009), and black for Nagao et al. (2006b). For the low-redshift measurements of Nagao et al. (2006b), their measurements for three different magnitude ranges ( $-29.5 \leq M_B \leq -28.5$ ,  $-27.5 \leq M_B \leq -26.5$ ,  $-25.5 \leq M_B \leq -24.5$ ) are separately plotted to show that brighter quasars in general show larger flux ratios. The Si III]  $\lambda 1892$  flux is added to the data points of Nagao et al. (2006b) for the C III]/C IV flux ratio (bottom right panel), because this weak line was not deblended in the other studies that are quoted in this figure. De Rosa et al. (2014) and Tang et al. (2019) are shown as open circles in the C III]/C IV panel, because those two studies fitted Al III+Si III]+C III] as a single line.

**Table 3**  
Emission-line Ratio

Continuum Model	Si II/C IV	Si IV/C IV	Al III/C IV	C III]/C IV	Fe II/Mg II
T06	$0.22^{+0.02}_{-0.02}$	$0.62^{+0.04}_{-0.05}$	$0.17^{+0.03}_{-0.03}$	$0.79^{+0.04}_{-0.06}$	$8.7^{+0.6}_{-1.3}$
VW01	$0.22^{+0.02}_{-0.02}$	$0.62^{+0.04}_{-0.04}$	$0.17^{+0.02}_{-0.03}$	$0.78^{+0.04}_{-0.05}$	$5.5^{+0.4}_{-0.8}$
T06_noBC	$0.26^{+0.02}_{-0.02}$	$0.66^{+0.05}_{-0.05}$	$0.17^{+0.04}_{-0.03}$	$0.75^{+0.05}_{-0.06}$	$7.7^{+0.6}_{-0.9}$
T06_wide	$0.19^{+0.02}_{-0.01}$	$0.55^{+0.03}_{-0.03}$	$0.16^{+0.03}_{-0.02}$	$0.71^{+0.04}_{-0.04}$	$1.4^{+0.4}_{-0.6}$

**Note.** The emission-line ratios are shown for four different models: “T06” and “VW01” denote the (power-law and Balmer) continuum+iron+emission-line fits in which the iron templates of Tsuzuki et al. (2006) and Vestergaard & Wilkes (2001) are used, respectively. “T06\_noBC” denotes the model in which the Tsuzuki et al. (2006) template was used but only the power-law continuum was fitted for the continuum component. “T06\_wide” is the model in which the spectrum is fitted with the same components as those of the T06 model but with a wider continuum+iron window (see Section 5.1 for more details).

Fe III multiplet at  $\lambda_{\text{rest}} \approx 1900 \text{ \AA}$  (Vanden Berk et al. 2001; Vestergaard & Wilkes 2001), which was just considered by scaling the iron templates with the factor determined at

the Fe II multiplet at  $\lambda_{\text{rest}} = 2500\text{--}2890 \text{ \AA}$ . Therefore, it is not clear whether the apparently high C III]/C IV line ratio and the large scatter at  $z \gtrsim 6$  (as was also pointed out by

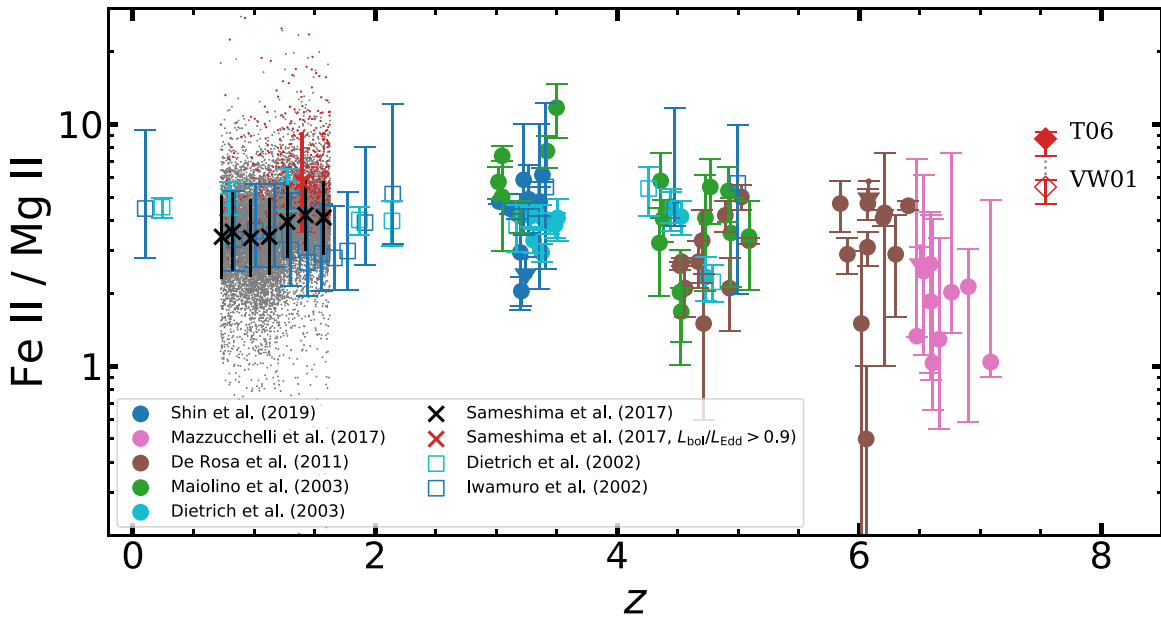


**Figure 5.** Fe II/Mg II line ratios as a function of redshift. Red diamonds show ULAS J1342+0928, with the different symbols corresponding to different iron templates used in the spectral decomposition (filled symbol: T06; open symbol: VW01). The colored circles show the Fe II/Mg II measurements of individual quasars in the literature: Dietrich et al. (2003a; cyan), Maiolino et al. (2003; green), De Rosa et al. (2011; brown), Mazzucchelli et al. (2017; magenta), and Shin et al. (2019; blue). The SDSS DR7 quasars at  $0.72 < z < 1.63$  from Sameshima et al. (2017) are shown as dots. Their median Fe II/Mg II flux ratios binned by redshift ( $\Delta z = 0.15$ ) are shown as black crosses, with the error bars showing standard deviation. The low-redshift SDSS quasars with the Eddington ratios over  $L_{\text{bol}}/L_{\text{Edd}} = 0.9$  (comparable to ULAS J1342+0928) are shown as red dots, with the median of this subsample shown as a red cross. Open squares show the redshift evolution down to  $z \sim 5$  based on the median values compiled by Iwamuro et al. (2002; blue) and composite spectra constructed by Dietrich et al. (2002b; cyan). For the latter measurement, the Fe II/Mg II values presented in Dietrich et al. (2003a) are quoted.

De Rosa et al. 2014) reflect intrinsic changes in the C III] emission line or are due to the complex line blending of C III] with Al III, Si III], and Fe III.

Venemans et al. (2017b) and Novak et al. (2019) investigated the host galaxy properties of ULAS J1342+0928 by rest-frame FIR dust continuum and atomic emission lines from the interstellar medium (ISM). They revealed that the host galaxy has a high star formation rate ( $\sim 150 M_{\odot} \text{yr}^{-1}$ ) and that its ISM is rich in dust ( $M_{\text{dust}} = 3.5 \times 10^7 M_{\odot}$ ). The line ratio of the rest-frame FIR [O III] 88  $\mu\text{m}$  and [N II] 122  $\mu\text{m}$  emission lines suggested that the ISM gas-phase metallicity is consistent with the solar value. Therefore, ULAS J1342+0928 experienced rapid metal enrichment over both the BLR (subparsec) and the ISM (kpc) scales.

#### 4.4. Fe II/Mg II

The Fe II/Mg II flux ratio has been used as a proxy for the Fe/ $\alpha$ -element abundance ratios in the BLR clouds. The Fe II/Mg II line ratio of ULAS J342+0928 is  $\text{Fe II/Mg II} = 8.7_{-1.3}^{+0.6}$  (for the T06 model) as reported in Table 3. The VW01 model gives a smaller value with  $\text{Fe II/Mg II} = 5.5_{-0.8}^{+0.4}$ . This difference is due to the overestimated Mg II flux in the VW01 iron template, as revisited in Section 5.1. In Figure 5, the Fe II/Mg II measurements in the literature are compiled as a function of redshift, in which both the T06 and VW01 models are shown for ULAS J1342+0928. The filled circles at  $3 \lesssim z \lesssim 7$  show the measurements of individual quasars (Dietrich et al. 2003a; Maiolino et al. 2003; De Rosa et al. 2011; Mazzucchelli et al. 2017; Shin et al. 2019). Since the same quasars are frequently used in more than one paper, only the most recent measurements are shown in Figure 5 to avoid sample duplication. For the low-redshift quasars, the Fe II/Mg II values of the individual SDSS DR7 quasars from Sameshima et al. (2017) are shown with their

median values binned by redshift (with a step of  $\Delta z = 0.15$ ). The redshift average over  $0.1 < z < 5.0$  reported in Iwamuro et al. (2002) and the Fe II/Mg II values of the composite spectra at  $0.2 \leq z \leq 4.8$  that were constructed by Dietrich et al. (2002b) are compared with the SDSS quasars in Figure 5.

ULAS J1342+0928 is apparently as iron-rich as the lower-redshift quasars, as its Fe II/Mg II line ratio is comparable to the  $z \lesssim 7$  quasars. However, comparison with those measurements in the literature is not simple, because they often use different methods to model the quasar continuum and iron forests. For example, many of the  $z \gtrsim 6$  quasars were measured with the VW01 iron template (Jiang et al. 2007; De Rosa et al. 2011; Mazzucchelli et al. 2017), while Sameshima et al. (2017) use the T06 template for their low-redshift quasars. Shin et al. (2019) applied both the VW01 and T06 templates.<sup>19</sup> The Fe II/Mg II line ratio gets 0.20 dex smaller when the Vestergaard & Wilkes (2001) model is applied to ULAS J1342+0928 ( $\text{Fe II/Mg II} = 5.5_{-0.8}^{+0.4}$ ), in which case the line ratio is closer to the  $z \gtrsim 6.5$  quasars in Mazzucchelli et al. (2017). The systematic uncertainty in the Fe II/Mg II measurement is further discussed in Section 5.1. In either case, our deep observation of ULAS J1342+0928 suggests rapid iron enrichment in the BLR clouds at  $z > 7.54$ .

Moreover, photoionization calculations suggest that the strengths of the Fe II and the Mg II emission lines are affected by nonabundance parameters, such as the BLR gas density and the microturbulence within the gas clouds (e.g., Verner et al. 1999; Baldwin et al. 2004; Dong et al. 2011; Sameshima et al. 2017). Sameshima et al. (2017) showed that the gas density is the dominant nonabundance parameter that changes the Fe II/Mg II line ratio. This argument is based on the fact in their

<sup>19</sup> Their latter model is quoted in Figure 5 to be consistent with our measurement of ULAS J1342+0928.

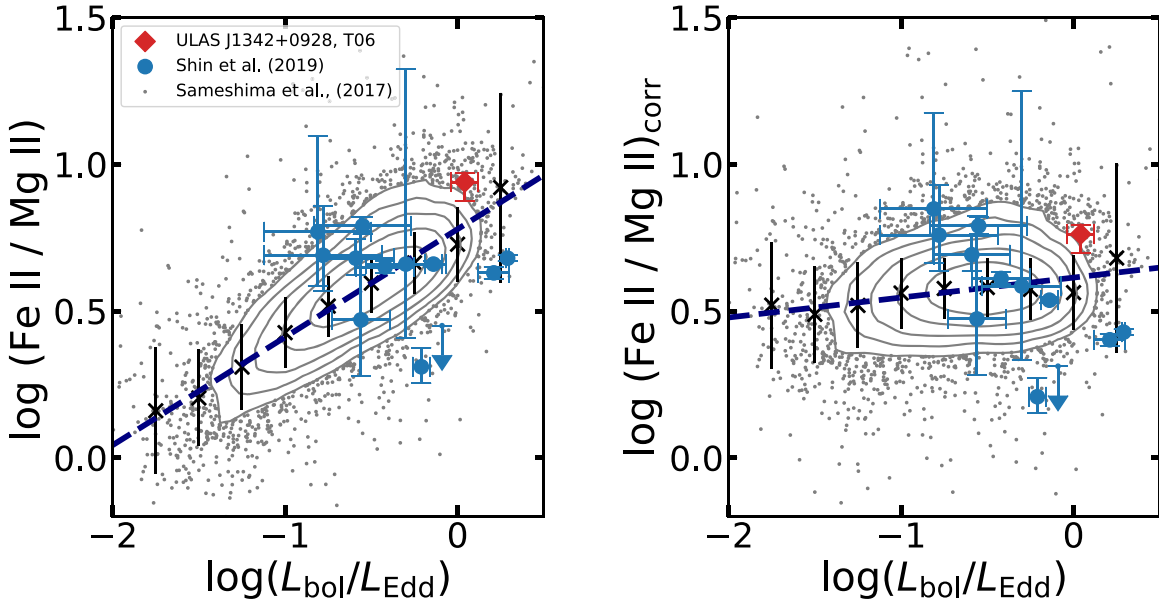


**Figure 6.** Left: dependence of the Fe II/Mg II line ratio on the Eddington ratio. Symbols are the same as Figure 5, while only the measurements using the Tsuzuki et al. (2006) iron template are shown in this plot. The lognormal local densities of the SDSS DR7 quasars are shown in gray contours with a grid size of 0.3 dex. For the SDSS DR7 quasars, their median and standard deviation at small bins ( $\Delta \log(L_{\text{bol}}/L_{\text{Edd}}) = 0.25$  dex) are also shown as crosses, with the dashed line being the linear regression to the distribution (Sameshima et al. 2017). Right: same as the left panel, but with the Fe II/Mg II line ratio corrected for the Eddington ratio dependence given in Sameshima et al. (2017):  $\log(\text{Fe II}/\text{Mg II})_{\text{corr}} = \log(\text{Fe II}/\text{Mg II}) - 0.30(\log(L_{\text{bol}}/L_{\text{Edd}}) + 0.55)$ .

photoionization model that the two emission lines originate from different regions inside the BLR gas clouds.

The left panel of Figure 6 shows the Fe II/Mg II– $L_{\text{bol}}/L_{\text{Edd}}$  plane, in which only the measurements using the T06 iron template are shown (i.e., Sameshima et al. 2017; Shin et al. 2019; this study) to avoid scatters due to different choice of iron templates. In this figure, it is clear that the low-redshift SDSS quasars have a positive correlation between Fe II/Mg II and the Eddington ratio. While ULAS J1342+0928 has an approximately twice higher Fe II/Mg II ratio than the median value of the entire low-redshift quasars, the  $z < 2$  SDSS quasars at the near or super-Eddington range ( $L_{\text{bol}}/L_{\text{Edd}} > 0.9$ ) have similar Fe II/Mg II ratios to ULAS J1342+0928. Those low-redshift counterparts are also shown as red dots in Figure 5. In order to better trace the relative iron abundance over magnesium (i.e.,  $\alpha$ -element) in the BLR clouds, Sameshima et al. (2017) introduced the correction to the Eddington ratio dependence of the Fe II/Mg II ratios:

$$\text{EW}(\text{Mg II})_{\text{corr}} = \text{EW}(\text{Mg II}) \left( \frac{\langle L_{\text{bol}}/L_{\text{Edd}} \rangle}{L_{\text{bol}}/L_{\text{Edd}}} \right)^{-0.30}, \quad (2)$$

where the normalization factor is  $\langle L_{\text{bol}}/L_{\text{Edd}} \rangle = 10^{-0.55}$ . The corrected Fe II/Mg II– $L_{\text{bol}}/L_{\text{Edd}}$  plane in the right panel of Figure 6 has a smaller scatter over the entire Eddington ratio range. ULAS J1342+0928 with the corrected  $(\text{Fe II}/\text{Mg II})_{\text{corr}} = 5.8_{-0.9}^{+0.4}$  now has a less extreme Fe II/Mg II with only a  $1.6\sigma$  excess from the median of the entire low-redshift SDSS quasars. Therefore, this correction gives strong evidence that the iron enrichment is completed at  $z > 7.54$  (i.e., when the universe is less than 680 million years old), at least in the scale where the local chemical abundance is represented by the BLR clouds. Further discussions are provided in Section 5.2 about the early iron enrichment.

#### 4.5. BH Mass

Our new Mg II line measurement enabled us to revisit the BH mass of ULAS J1342+0928. The scaling relation given in Vestergaard & Osmer (2009) was used as in our previous measurement (Bañados et al. 2018). The virial mass was derived with the following equation:

$$M_{\text{BH}} = 10^{6.86} \left( \frac{\text{FWHM}(\text{Mg II})}{10^3 \text{ km s}^{-1}} \right)^2 \left( \frac{\lambda L_{\lambda}(3000 \text{ \AA})}{10^{44} \text{ erg s}^{-1}} \right)^{0.5} M_{\odot}, \quad (3)$$

where  $\text{FWHM}(\text{Mg II})$  is the full width at half-maximum of the Mg II line and  $\lambda L_{\lambda}(3000 \text{ \AA})$  is the monochromatic luminosity at rest frame  $3000 \text{ \AA}$ . The measurement uncertainty of the virial BH mass was derived by propagating the measurement errors of the Mg II line width and the monochromatic luminosity. The systematic errors are usually larger than the measurement errors of the BH masses, as Shen (2013) argue that there is a 0.5 dex uncertainty in the Mg II-based mass measurements. A subsequently derived quantity after the  $M_{\text{BH}}$  measurement is the Eddington luminosity:

$$L_{\text{Edd}} = 1.3 \times 10^{38} \left( \frac{M_{\text{BH}}}{M_{\odot}} \right) \text{ erg s}^{-1}. \quad (4)$$

The Eddington ratio  $L_{\text{bol}}/L_{\text{Edd}}$  was derived by dividing the bolometric luminosity by the Eddington luminosity.

The resulting BH mass for ULAS J1342+0928 is  $M_{\text{BH}} = 9.1_{-1.4}^{+1.3} \times 10^8 M_{\odot}$  for the T06 model. The Eddington ratio is  $L_{\text{bol}}/L_{\text{Edd}} = 1.1_{-0.2}^{+0.2}$ . Only the measurement errors are taken into account in the reported uncertainties. The Mg II-based BH mass slightly increases from the previous measurement of  $M_{\text{BH}} = 7.6_{-1.9}^{+3.2} \times 10^8 M_{\odot}$  (Bañados et al. 2018), while the difference is within the  $1\sigma$  level of the previous measurement. Accordingly, the Eddington ratio decreases from  $L_{\text{bol}}/L_{\text{Edd}} = 1.5_{-0.4}^{+0.5}$  to a near-Eddington limit. The reason for this difference, albeit small,

is due to the wider Mg II width and the suppressed continuum luminosity by the additional iron pseudocontinuum considered in the spectral fitting.

The virial BH mass becomes even more massive when the VW01 model is used. As reported in Table 2, the Mg II width is 34% broader than that in the T06 model. The broader line profile increases the Mg II-based BH mass by a factor of 1.8 ( $M_{\text{BH}} = 1.6_{-0.2}^{+0.2} \times 10^9 M_{\odot}$ ), as the BH mass scales with  $\text{FWHM}(\text{Mg II})^2$  (Vestergaard & Osmer 2009) and the continuum luminosity does not change between the two models. This difference is still within the 0.5 dex systematic uncertainty of the Mg II-based mass measurements (Shen 2013). The Eddington ratio becomes  $L_{\text{bol}}/L_{\text{Edd}} = 0.60_{-0.07}^{+0.08}$  in this case.

Our updated mass measurement confirms that ULAS J1342+0928 is powered by a matured and actively accreting SMBH at the Eddington limit, which poses a question to the formation and early growth scenario of the SMBHs in the early universe (e.g., Inayoshi et al. 2020).

## 5. Discussion

### 5.1. Systematic Uncertainties on Mg II and Fe II Measurements

There are offsets in the measured Fe II/Mg II flux ratios in the literature, even at the same redshift and Eddington ratio ranges. Previous studies argued that the offsets at least partly originated from systematic uncertainties of the Mg II and Fe II line measurements, which could be up to a factor of two and more (Kurk et al. 2007; De Rosa et al. 2011, 2014; Shin et al. 2019). For example, SDSS J1030+0524 at  $z = 6.3$  (Fan et al. 2001) has a number of Fe II/Mg II measurements based on different observations and methods, with the reported values ranging from Fe II/Mg II = 0.99 to 8.65 (Freudling et al. 2003; Maiolino et al. 2003; Iwamuro et al. 2004; Jiang et al. 2007; Kurk et al. 2007; De Rosa et al. 2011). This section explores how the Fe II/Mg II measurement using the deep spectrum of ULAS J1342+0928 is affected by different fitting approaches.

First, different iron templates affect total Mg II flux and line profile, while this is not the case for the other emission lines at the bluer side (Table 2). Figure 7 shows the continuum-subtracted spectrum at  $\lambda_{\text{rest}} = 2500\text{--}2900 \text{ \AA}$ , where the best-fit Fe II and Mg II components are compared between the T06 and the VW01 models. Figure 8 also shows the two models with the decomposed spectral components (i.e., power-law continuum, Balmer continuum, iron template, and single Gaussian for the Mg II line) at the same wavelength range. The difference of the power-law+Balmer continuum components at this region is tiny between the two models, compared to flux errors. As already mentioned in Section 3.2, the difference between the two iron templates is the iron contribution underneath the Mg II line, where Tsuzuki et al. (2006) compensated the oversubtracted Fe II flux with their photoionization simulation. The T06 model results in a narrower Mg II line profile and a smaller equivalent width than the VW01 model ( $\text{FWHM} = 2830_{-210}^{+210} \text{ km s}^{-1}$  and  $\text{EW}_{\text{rest}} = 13.4_{-0.9}^{+0.8} \text{ \AA}$  for T06, and  $\text{FWHM} = 3780_{-260}^{+220} \text{ km s}^{-1}$  and  $\text{EW}_{\text{rest}} = 19.9_{-1.5}^{+0.7} \text{ \AA}$  for VW01), while in both cases the line width is broader than that measured in Bañados et al. (2018;  $\text{FWHM} = 2500_{-320}^{+480} \text{ km s}^{-1}$ ). The difference due to different iron templates is also found in the Mg II blueshift. The residual spectra after subtracting the best-fit continuum and iron templates are compared in the bottom panel of Figure 7. The Mg II line center in the T06 model has a smaller blueshift ( $\Delta v_{\text{Mg II}-[\text{C II}]} = 340_{-80}^{+110} \text{ km s}^{-1}$ ) than in the VW01 model

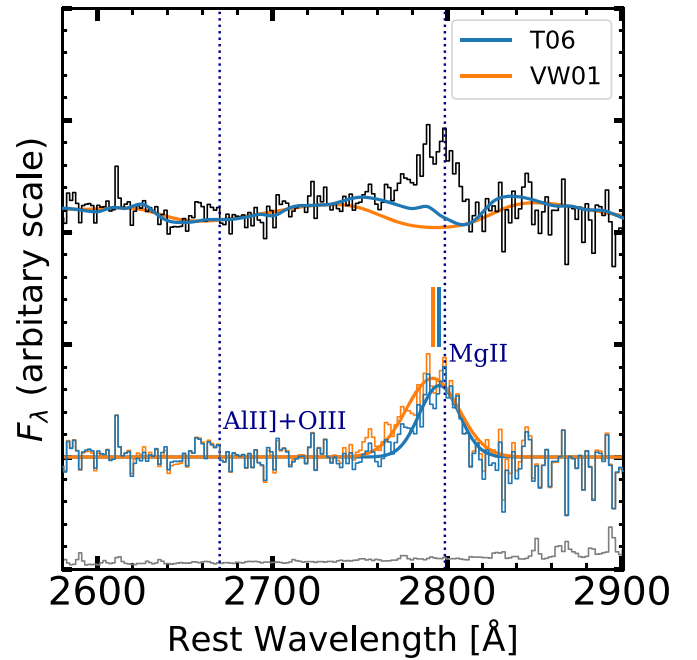


**Figure 7.** Top: continuum (power-law and Balmer) subtracted spectrum around the Mg II line (black). The best-fit iron pseudo-continua from the T06 and VW01 models are shown in blue and orange, respectively. Bottom: same spectrum after Fe II subtraction. The best-fit single Gaussian profile and the line center of Mg II are shown for each model. The flux excess visible at  $\lambda_{\text{rest}} \approx 2670$  is from the blended and blueshifted Al III+O III  $\lambda 2672$ . The rest-frame wavelengths of Mg II and the Al III+O III composite are indicated by vertical dotted lines. The flux error at each pixel is indicated by the gray line at the bottom.

( $\Delta v_{\text{Mg II}-[\text{C II}]} = 750_{-90}^{+90} \text{ km s}^{-1}$ ). This is because of the asymmetric profile of the iron forest underneath Mg II (see Figure 7). As a result, there is more remaining flux in the VW01 model at the blue side of the emission line after the iron subtraction, which enhances the Mg II flux by  $47_{-11}^{+11}\%$  and reduces Fe II/Mg II (Table 3). This systematic effect on the Mg II measurement caused by different iron templates was also discussed in the literature for other sources (e.g., Kurk et al. 2007; Woo et al. 2018; Shin et al. 2019).

Another factor that affects the emission-line measurements is the fitting procedure of the quasar power-law and Balmer continuum. As mentioned in Section 3, the Balmer continuum is degenerate with the power-law continuum and the Fe II pseudo-continuum at the wavelength range of the GNIRS spectrum. The Balmer continuum is tied to the power-law continuum in our spectral modeling, with its scaling factor fixed to 30% of the power-law flux at  $\lambda_{\text{rest}} = 3675 \text{ \AA}$ . The electron temperature and the optical depth were fixed to  $T_e = 15,000 \text{ K}$  and  $\tau = 1$ , as De Rosa et al. (2014) argued that directly fitting those two parameters does not make a significant impact on the Fe II/Mg II measurements.

In order to address the robustness of those assumptions and the potential impacts on the Fe II/Mg II measurements, different Balmer continuum models were tested with our GNIRS spectrum of ULAS J1342+0928 by changing the normalization factor to 0%–100%.<sup>20</sup> The electron temperature and optical depth were fixed to the same values as in the original model.

<sup>20</sup> The scaling factors of the Balmer continuum used in this test were 0, 0.01, 0.03, 0.04, 0.05, 0.1, 0.3, 0.4, 0.5, and 1 with respect to  $F_{\text{PL}}^{\text{PL}}$  at  $\lambda_{\text{obs}} = 3675(1+z) \text{ \AA}$ . The 0% model corresponds to our T06\_noBC model.

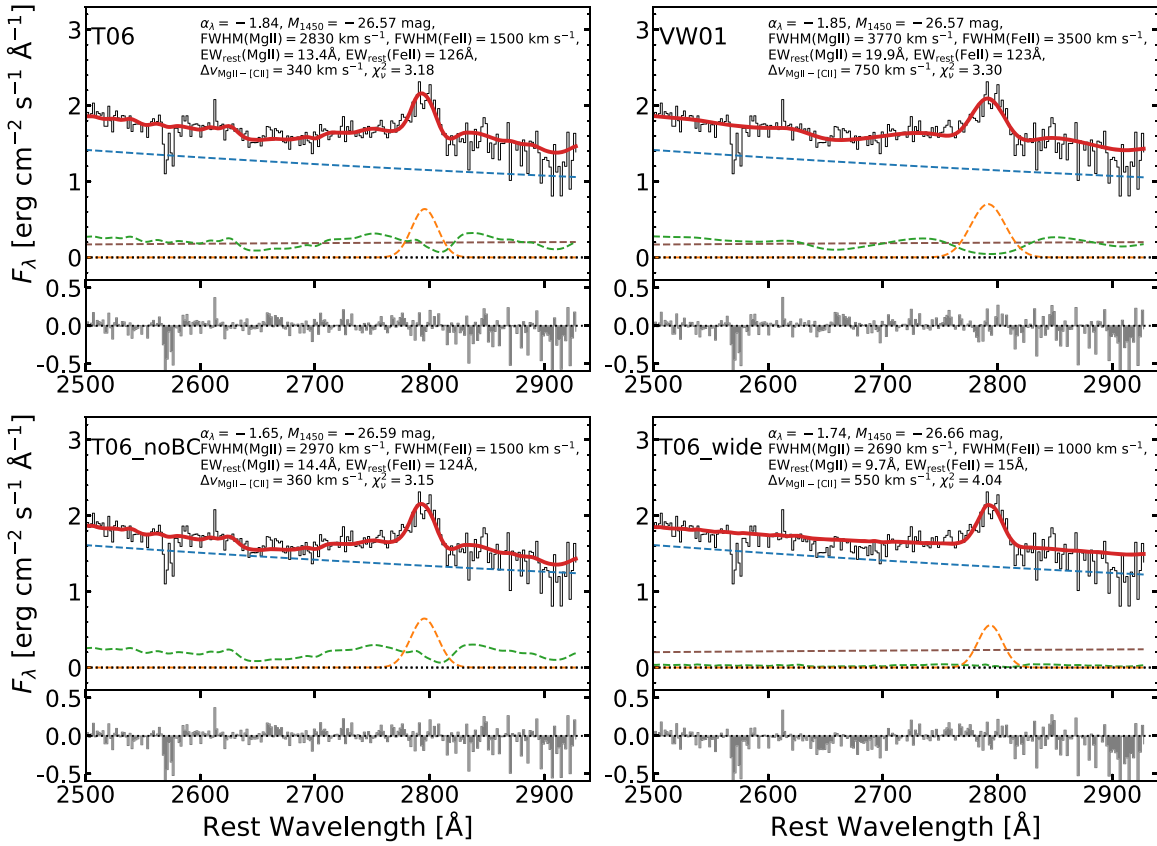


**Figure 8.** Comparison of four different spectral models described in Section 5.1 (see Table 3). The observed spectrum is the same as the one presented in Figure 1, while the residual fluxes of the fit are also shown in the bottom panel. The name of the model is indicated at the top left of each panel. The colors of the lines are the same as in Figure 1, while the best-fit single Gaussian for Mg II is also shown in orange. In each model, the best-fit emission-line and continuum parameters and reduced chi-square of the multicomponent (continuum+iron+Mg II) fit at  $\lambda_{\text{rest}} = 2500\text{--}2900$  Å are shown inside each panel. Note that a  $z = 6.86$  Mg II doublet absorption is at  $\lambda_{\text{rest}} = 2580$  Å, which was reported in Cooper et al. (2019).

Different values of the two parameters were also tested, but their impacts on the emission-line measurements are smaller than those of the normalization, confirming the test done by De Rosa et al. (2014). The broad emission lines were fitted with the same procedure applied to our fiducial model with the **T06** iron template. As a result, the GNIRS spectrum was well fitted when the normalization factors were  $\leq 30\%$ , as the goodness of the joint continuum and iron fitting at the Fe II windows becomes slightly better ( $-0.02 \lesssim \Delta\chi^2_\nu \lesssim 0$ ). The reduced chi-square got worse when the normalization factor was higher ( $>30\%$ ) up to  $\Delta\chi^2_\nu = 0.3$ , as the Fe II forest was poorly fitted owing to the stronger-than-necessary Balmer continuum at  $\lambda_{\text{rest}} \gtrsim 2200$  Å. Therefore, it is likely that the actual contribution of the Balmer continuum is 30% or lower, while the exact amount is beyond the scope of this paper.

The resulting range of the Fe II/Mg II values is  $7.8 \leq \text{Fe II/Mg II} \leq 8.7$ , with the minimum value obtained when the normalization is 3%–5%. Those models actually give the minimum chi-square in the continuum+iron fitting, while the deviation from the fiducial 30% model is within the  $1\sigma$  uncertainty ( $\text{Fe II/Mg II} = 8.7^{+0.6}_{-1.3}$ ). Therefore, the 0%–30% normalization gives adequate spectral decomposition and a reliable measurement of Fe II/Mg II for ULAS J1342+0928. In Table 3, the flux ratios of the power-law-only continuum model dubbed as “T06\_noBC” are reported to represent the “weak Balmer continuum” models. The best-fit spectral decomposition in the T06\_noBC model is also shown in Figure 8. In this case, the power-law slope gets flatter ( $\alpha_\lambda = -1.65^{+0.02}_{-0.01}$ ), with little change in the absolute magnitude

( $M_{1450} = -26.59 \pm 0.04$ ). The Fe II/Mg II line ratio decreases by 11% ( $\text{Fe II/Mg II} = 7.7^{+0.6}_{-0.9}$ ), which is within the  $1\sigma$  uncertainty of the **T06** model. This small change indicates that the assumption on the Balmer continuum strength is a relatively small factor that introduces systematic uncertainties in the Fe II and Mg II flux measurements.

On the other hand, the continuum window used in fitting the power-law continuum has a bigger impact on the Mg II and Fe II measurements. In our original **T06** modeling, the following emission-line-free regions were chosen:  $\lambda_{\text{rest}} = 1275\text{--}1285$  Å, 1310–1325 Å, 2500–2750 Å, and 2850–2890 Å (Section 3.3). Only a small region of the quasar continuum is used at the blue side because most parts of the observed wavelengths are covered with the extremely broad emission lines of ULAS J1342+0928 ( $\text{FWHM} > 10,000$  km s<sup>-1</sup> for high-ionization lines; Table 2). The same spectral fitting was performed with a wider continuum window to test how the Fe II/Mg II line ratio is sensitive to the continuum fitting (“T06\_wide” model in Table 3). Three additional wavelength ranges,  $\lambda_{\text{rest}} = 1425\text{--}1470$  Å, 1680–1710 Å, and 1975–2050 Å, were added to the original continuum window. Also, the second reddest window was extended from 2500–2750 Å to 2260–2750 Å to cover the entire UV Fe II bump. Those regions are in fact not line-free. The observed flux deviates from the power-law component at  $\lambda_{\text{rest}} \approx 1600\text{--}1800$  Å in the composite spectra of low-redshift quasars (Vanden Berk et al. 2001; Nagao et al. 2006b). The rest frame  $\lambda_{\text{rest}} = 1425\text{--}1470$  Å is usually a line-free region, but the extremely broad outskirts of the Si IV and C IV emission lines in ULAS J1342+0928 likely

contribute to the observed flux in this region (see Figure 1). There are Fe III emission lines at  $\lambda_{\text{rest}} \sim 2000 \text{ \AA}$ .

As a result, the power-law continuum becomes brighter than the T06 model by  $\Delta M_{1450} = -0.09 \text{ mag}$ , with a flatter slope of  $\alpha_{\lambda} = -1.74^{+0.01}_{-0.01}$ . More importantly, the higher continuum level largely suppresses the iron contribution (Figure 8). The total Fe II flux becomes only 14% of the one in the T06 model, which results in a smaller line ratio of  $\text{Fe II}/\text{Mg II} = 1.4^{+0.4}_{-0.6}$ . This model better traces the observed flux at  $\lambda_{\text{rest}} \approx 1700$  and  $\approx 2000 \text{ \AA}$ , while parts of the flux in those regions are from the unidentified weak emission lines. This model poorly traces the Fe II bump compared to the other three models. The reduced chi-square of the continuum+iron+Mg II line fitting at  $\lambda_{\text{rest}} = 2500\text{--}2900 \text{ \AA}$  gets worse by  $\Delta\chi_{\nu} = 0.86$  from the T06 model. The T06 model (and also the VW01 and T06\_noBC models) reproduces the UV Fe II bump, while the T06\_wide model roughly fits this feature only with the power-law continuum. This overestimated continuum level of the T06\_wide model also affects the other emission lines at bluer sides, while the effect is smaller than that for Fe II/Mg II. As reported in Table 3, the emission-line ratios other than Fe II/Mg II also decrease from the T06 model by  $\leq 11\%$ .

Overall, good care should be taken in the continuum and iron modeling, especially when Fe II/Mg II is to be measured from a quasar spectrum. Although not addressed in this section, there are other factors that potentially affect the Fe II/Mg II measurements, such as whether or not the blueshifts of the iron emission lines are considered. Previous studies reported large Fe II/Mg II scatters even at the same redshift and luminosity ranges, with some quasars showing very small Fe II/Mg II ratios ( $\text{Fe II}/\text{Mg II} \ll 1$ ; Mazzucchelli et al. 2017; Shin et al. 2019). Those results may indicate that there is a variation in the iron abundance and the iron enrichment is ongoing in some quasars at  $z \lesssim 7$ . However, given the large effects that different spectral modeling approaches have on the Fe II/Mg II measurements as presented in this section, it is important to revisit the early iron enrichment by measuring Fe II/Mg II for a large sample of quasars spanning over a wide redshift range based on a unified approach.

### 5.2. Early Iron Enrichment

The BLR gas-phase metallicity traces the star formation history of the host galaxies of quasars, as the BLR gas originated from the ISM of the host galaxies falling onto the nuclear regions. Previous studies show that the BLR clouds have supersolar metallicity up to  $z \sim 7$  (e.g., Nagao et al. 2006b; Jiang et al. 2007; De Rosa et al. 2014; Xu et al. 2018; Tang et al. 2019). Moreover, the lack of redshift evolution in the Fe II/Mg II line ratios (with a large scatter) indicates rapid iron enrichment with respect to the  $\alpha$ -elements within the first billion years of the universe (e.g., Jiang et al. 2007; De Rosa et al. 2014; Mazzucchelli et al. 2017). This trend holds for ULAS J1342+0928 at  $z = 7.54$  (Sections 4.3 and 4.4).

While SNe Ia have a higher iron production efficiency than SNe II, the SN Ia explosions are delayed from the initial starburst. This time delay is due to the timescale required for formation of white dwarfs and mass transfer from their companion stars or mergers due to the loss of orbital energy by gravitational wave radiation (Maoz et al. 2014). For a star with a mass a few times solar to explode as an SN Ia, the time delay is  $\sim 1 \text{ Gyr}$  (Greggio & Renzini 1983), while the minimum

time delay is  $\sim 40 \text{ Myr}$ , which corresponds to the main-sequence lifetime of an  $8M_{\odot}$  star.

The recent observational constraints on the SN Ia rate as a function of times between starbursts and explosion (or so-called delay-time distribution) favor a power-law shape with a slope of  $t^{-1}$  over  $t \approx 0.1\text{--}10 \text{ Gyr}$  (e.g., Maoz & Mannucci 2012; Maoz et al. 2014, and references therein).<sup>21</sup> Rodney et al. (2014) suggest that about half of the SNe Ia explode within 500 Myr. Therefore, given the young age of the universe when ULAS J1342+0928 was observed (680 Myr), it is likely that those prompt SNe Ia contributed to the iron enrichment of the host ISM.

It is useful to estimate approximately how many SNe Ia and SNe II are needed to explain the early iron enrichment in the BLR gas. Here, the BLR gas clouds are assumed to be  $10^4 M_{\odot}$  (Baldwin et al. 2003) with  $5Z_{\odot}$  metallicity (Nagao et al. 2006b). If the relative mass fraction of metal elements is the same as the solar system (Asplund et al. 2009), the magnesium and iron masses in the BLR are  $36M_{\odot}$  and  $65M_{\odot}$ , respectively. Based on the SN Ia yields of Iwamoto et al. (1999)<sup>22</sup> and SN II yields of Nomoto et al. (2013), those masses can be achieved with  $\sim 60$  SNe Ia and  $\sim 200$  SNe II of  $20M_{\odot}$  stars with zero to supersolar metallicity ( $Z = 0\text{--}0.05$ ). Pair-instability SNe (PISNe) could also significantly contribute to the iron enrichment if the Population III stars are as massive as  $140 < M/M_{\odot} < 260$ . A total of  $7M_{\odot}$  of iron is ejected from a metal-free  $200M_{\odot}$  star through PISNe in this case (Nomoto et al. 2013).

However, more SNe should have been responsible for the high BLR metallicity than the numbers given above. The chemical enrichment of the BLR gas is tied to the host star formation at a much larger scale than the actual BLR size, because the BLR gas likely originated from the host ISM inflowing onto the central SMBH. A nonnegligible fraction of the metal-polluted SNe remnants are consumed in the subsequent star formation and thus do not remain as gas. Moreover, the BLR gas with  $10^{3\text{--}4} M_{\odot}$  only accounts for a tiny fraction of the mass at the nuclear region, given the central SMBH mass of  $M_{\text{BH}} \sim 10^9\text{--}10^{10} M_{\odot}$  for a luminous quasar such as those known at  $z > 6$ . Therefore, it is more realistic that the high BLR metallicity reflects far more than 10–100 SNe, and as Baldwin et al. (2003) concluded, the rapid chemical enrichment of the BLR gas should trace the star formation history of the quasar host galaxies at the scale where the local ISM is tied to the SMBH feeding.

## 6. Summary and Conclusion

### 6.1. Summary of This Work

The BLR properties of ULAS J1342+0928 at  $z = 7.54$  were measured with a deep (9 hr on source) NIR spectrum taken by Gemini/GNIRS at  $\lambda_{\text{rest}} = 970\text{--}2930 \text{ \AA}$ . The spectrum was modeled by a combination of a power-law continuum, a Balmer continuum, and templates of UV iron (Fe II+Fe III) pseudo-continuum. Various emission lines are then modeled by single Gaussian profiles after subtracting those continuum components, namely, Si II  $\lambda 1263$ , Si IV  $\lambda 1397$ , C IV  $\lambda 1549$ , Al III  $\lambda 1857$ , C III]  $\lambda 1909$ , and Mg II  $\lambda 2798$ . The line flux of the  $\text{Ly}\alpha + \text{N V } \lambda 1240$  composite was instead measured by summing

<sup>21</sup> According to the SN Ia rate given in Maoz & Mannucci (2012, Equation (13)), the number of SNe Ia between 40 and 680 Myr is  $10^7$  SNe per  $10^{10} M_{\odot}$  host stellar mass.

<sup>22</sup> The SN Ia yields quoted here are based on their W7 model.

the flux above the continuum at  $\lambda_{\text{rest}} = 1160\text{--}1290 \text{ \AA}$ . NV  $\lambda 1240$  and He II  $\lambda 1640$  were not identified as individual lines owing to their heavy line blending, weakness, atmospheric absorption, and the strong IGM absorption (for NV).

ULAS J1342+0928 exhibits large blueshifts with respect to its systematic redshift from the [C II] 158  $\mu\text{m}$  line. The amount of blueshifts has a linear correlation with the ionization potentials up to  $\Delta v_{[\text{C II}]} = 5510^{+240}_{-110} \text{ km s}^{-1}$  that is observed for C IV. The high-ionization emission lines also show broader profiles than those of low-ionization emission lines with FWHM more than  $10,000 \text{ km s}^{-1}$ . Those velocity offsets are remarkably larger than the average of  $z \sim 6\text{--}7$  quasars compiled in Shen et al. (2019) and Meyer et al. (2019), suggesting extreme outflow components in the BLR clouds.

The virial BH mass measurement was revised from Bañados et al. (2018) based on the multiple-component fit in this work. The Mg II-based BH mass based on our T06 model is  $M_{\text{BH}} = 9.1^{+1.3}_{-1.4} \times 10^8 M_{\odot}$ , with an Eddington ratio of  $L_{\text{bol}}/L_{\text{Edd}} = 1.1^{+0.2}_{-0.2}$ . This result confirms that ULAS J1342+0928 is powered by an already-matured SMBH actively accreting at the near-Eddington accretion rate.

The measured emission-line ratios, namely, Si II/C IV, Si IV/C IV, Al III/C IV, and C III/C IV, suggest that the BLR gas of ULAS J1342+0928 had a supersolar metallicity when the age of the universe was only 680 Myr. While the BLR gas-phase metallicity traces the past star formation at the galaxy center, this picture is consistent with the dust-rich and near-solar-metallicity ISM of the host galaxy revealed by the rest-FIR observations of the host galaxy (Venemans et al. 2017b; Novak et al. 2019).

The Fe II/Mg II emission-line ratio, a tracer of iron enrichment in the early universe, is also comparable to those of the lower-redshift quasars (Fe II/Mg II =  $8.7^{+0.6}_{-1.3}$ ). The Fe II/Mg II becomes even more typical when its Eddington ratio dependence is taken into account (Sameshima et al. 2017). Our result is somewhat in conflict with the predictions of SN Ia nucleosynthesis, the timescale of which is  $\sim 1 \text{ Gyr}$ . Prompt SNe Ia (and perhaps PISNe) that exploded within  $< 680 \text{ Myr}$  from the first star formation would have contributed to the early iron enrichment at the galaxy center. The nonevolution trend seen in the BLR line ratios, including Fe II/Mg II, should reflect the early metal enrichment at a much wider scale than the BLR itself, where the local ISM of the host galaxy is tied to the SMBH feeding.

There are a number of factors that introduce systematic errors in the Fe II/Mg II measurements. Four models with different iron templates (empirical templates from Tsuzuki et al. 2006 and Vestergaard & Wilkes 2001), continuum components (power-law plus Balmer continuum, or power-law only), and wavelength ranges at which the spectrum is fitted were tested to investigate how much the Fe II/Mg II value of ULAS J1342+0928 is sensitive to the fitting methods. As a result, not only the choice of iron templates, which has been discussed in the literature, but also the continuum window has a significant impact on Fe II/Mg II. The contribution of the quasar continuum is overestimated if it is fitted at the wavelength regions where weak and individually unidentified emission lines are present. The Fe II flux is underestimated in this case, which potentially explains the relatively low Fe II/Mg II ratios reported in the literature at high redshift. Given the large offsets that different fitting approaches introduce, one should measure the Fe II/Mg II line ratios with a unified

approach over a wide redshift range to address the potential fluctuation of the iron abundance in the BLR clouds. The Eddington ratio dependence of Fe II/Mg II should also be corrected to translate the line ratio to the actual abundance ratio, as introduced by Sameshima et al. (2017).

## 6.2. Future Prospects

There is apparently no redshift evolution in the BLR properties up to  $z = 7.54$ , except the BLR blueshifts (Section 4.2). The BLR studies of even higher-redshift (i.e.,  $z \gg 8$ ) quasars are required to identify the epoch when the BLR clouds were metal polluted to the supersolar metallicity. One caveat in the previous and the present studies is that most of the studies at high redshift are biased toward luminous quasars at each epoch. There is an indirect correlation between the UV luminosity of quasars and their host metallicity (e.g., Matsuoka et al. 2011b). Those two quantities are tied through the relation between SMBH and host bulge mass and the mass-metallicity relation of star-forming galaxies. In other words, studies on luminous quasars selectively sample massive SMBHs, the host galaxies of which are also presumably massive. The host galaxies of  $z \gtrsim 6$  luminous quasars have a dynamical mass of  $M_{\text{dyn}} \sim 10^{11} M_{\odot}$  (e.g., Decarli et al. 2018). Such matured galaxies would have already experienced chemical enrichment through their past star formation compared to lower-mass galaxies at the same redshift.

In this sense, lower-luminosity quasars could be better targets to trace chemically young BLRs. Shin et al. (2019) was motivated by this expectation and measured the Fe II/Mg II ratios for  $z \sim 3$  quasars that are an order of magnitude fainter ( $L_{\text{bol}} \sim 10^{46.5} \text{ erg s}^{-1}$ ) than the ones in previous studies at the same redshift; however, they did not find any significant difference in Fe II/Mg II. At  $z \gtrsim 6$ , the attempts of finding low-luminosity quasars have been led by the optical wide-field survey of the Subaru/Hyper Suprime-Cam (e.g., Matsuoka et al. 2016, 2019b). This deep survey has revealed SMBHs at a less massive range ( $M_{\text{BH}} = 10^{7-9} M_{\odot}$ ; Onoue et al. 2019). The host galaxies of those HSC quasars also have a variety of dynamical mass down to  $M_{\text{dyn}} \sim 10^{10} M_{\odot}$  (Izumi et al. 2018, 2019). Therefore, the deep observations of those less extreme SMBH populations at  $z > 6$  have a potential to witness metal-poor BLRs, while the sensitivity of 30 m-class ground-based telescopes or next-generation large space telescopes are needed to detect weak emission lines from the faintest  $z = 6\text{--}7$  HSC quasars at  $M_{1450} \sim -22 \text{ mag}$  (the continuum level of which is  $\sim 10^{-19} \text{ erg s}^{-1} \text{ cm}^{-2} \text{ \AA}^{-1}$  in the observed frame).

Also interestingly, recent observations have identified a few luminous  $z \sim 6$  quasars that were observed possibly only after  $< 10^5 \text{ yr}$  from their ignition (Eilers et al. 2017). While their SMBHs are as massive as those of the other luminous quasars at the same redshift range ( $M_{\text{BH}} \sim 10^9 M_{\odot}$ ; Eilers et al. 2018), the young quasars could also be good targets for future observations to identify the less metal-enriched BLRs, if their host galaxies are also young and host metal-poor ISMs.

We are grateful to the referee for providing constructive comments on the manuscript. We thank the Gemini North staffs for executing our programs. We also thank H. Sameshima for providing us his data on the SDSS DR7 quasars. This work was supported by the ERC Advanced Grant 740246 ‘‘Cosmic gas.’’ F. Wang acknowledges the support provided by NASA through the NASA Hubble Fellowship grant No. HST-HF2-51448.001-A

awarded by the Space Telescope Science Institute, which is operated by the Association of Universities for Research in Astronomy, Incorporated, under NASA contract NAS5-26555.

The data presented in this paper are based on observations obtained at the Gemini Observatory (GN-2017A-DD-4, GN-2019A-FT-115). The Gemini Observatory is operated by the Association of Universities for Research in Astronomy, Inc., under a cooperative agreement with the NSF on behalf of the Gemini partnership: the National Science Foundation (United States), National Research Council (Canada), CONICYT (Chile), Ministerio de Ciencia, Tecnología e Innovación Productiva (Argentina), Ministério da Ciência, Tecnologia e Inovação (Brazil), and Korea Astronomy and Space Science Institute (Republic of Korea).

*Facilities:* Gemini-North (GNIRS).

*Software:* astropy (Astropy Collaboration et al. 2013).


### ORCID iDs

Masafusa Onoue  <https://orcid.org/0000-0003-2984-6803>

Eduardo Bañados  <https://orcid.org/0000-0002-2931-7824>

Chiara Mazzucchelli  <https://orcid.org/0000-0002-5941-5214>

Bram P. Venemans  <https://orcid.org/0000-0001-9024-8322>


Jan-Torge Schindler  <https://orcid.org/0000-0002-4544-8242>

Fabian Walter  <https://orcid.org/0000-0003-4793-7880>

Joseph F. Hennawi  <https://orcid.org/0000-0002-7054-4332>

Irham Taufik Andika  <https://orcid.org/0000-0001-6102-9526>

Frederick B. Davies  <https://orcid.org/0000-0003-0821-3644>

Roberto Decarli  <https://orcid.org/0000-0002-2662-8803>

Emanuele P. Farina  <https://orcid.org/0000-0002-6822-2254>

Knud Jahnke  <https://orcid.org/0000-0003-3804-2137>

Tohru Nagao  <https://orcid.org/0000-0002-7402-5441>

Nozomu Tominaga  <https://orcid.org/0000-0001-8537-3153>

Feige Wang  <https://orcid.org/0000-0002-7633-431X>

### References

- Asplund, M., Grevesse, N., Sauval, A. J., & Scott, P. 2009, *ARA&A*, 47, 481
- Astropy Collaboration, Robitaille, T. P., Tollerud, E. J., et al. 2013, *A&A*, 558, A33
- Baldwin, J. A., Ferland, G. J., Korista, K. T., Hamann, F., & Dietrich, M. 2003, *ApJ*, 582, 590
- Baldwin, J. A., Ferland, G. J., Korista, K. T., Hamann, F., & LaCluyzé, A. 2004, *ApJ*, 615, 610
- Bañados, E., Decarli, R., Walter, F., et al. 2015, *ApJL*, 805, L8
- Bañados, E., Novak, M., Neeleman, M., et al. 2019, *ApJL*, 881, L23
- Bañados, E., Venemans, B. P., Decarli, R., et al. 2016, *ApJS*, 227, 11
- Bañados, E., Venemans, B. P., Mazzucchelli, C., et al. 2018, *Natur*, 553, 473
- Barth, A. J., Martini, P., Nelson, C. H., & Ho, L. C. 2003, *ApJL*, 594, L95
- Boroson, T. 2005, *AJ*, 130, 381
- Carilli, C. L., Neri, R., Wang, R., et al. 2007, *ApJL*, 666, L9
- Clough, S. A., Shephard, M. W., Mlawer, E. J., et al. 2005, *JQSR*, 91, 233
- Coatman, L., Hewett, P. C., Banerji, M., et al. 2017, *MNRAS*, 465, 2120
- Cooper, T. J., Simcoe, R. A., Cooksey, K. L., et al. 2019, *ApJ*, 882, 77
- Davies, F. B., Hennawi, J. F., Bañados, E., et al. 2018, *ApJ*, 864, 142
- De Rosa, G., Decarli, R., Walter, F., et al. 2011, *ApJ*, 739, 56
- De Rosa, G., Venemans, B. P., Decarli, R., et al. 2014, *ApJ*, 790, 145
- Decarli, R., Walter, F., Venemans, B. P., et al. 2018, *ApJ*, 854, 97
- Diamond-Stanic, A. M., Fan, X., Brandt, W. N., et al. 2009, *ApJ*, 699, 782
- Dietrich, M., Appenzeller, I., Vestergaard, M., & Wagner, S. J. 2002a, *ApJ*, 564, 581
- Dietrich, M., Hamann, F., Appenzeller, I., & Vestergaard, M. 2003a, *ApJ*, 596, 817
- Dietrich, M., Hamann, F., Shields, J. C., et al. 2002b, *ApJ*, 581, 912
- Dietrich, M., Hamann, F., Shields, J. C., et al. 2003b, *ApJ*, 589, 722
- Dong, X.-B., Wang, J.-G., Ho, L. C., et al. 2011, *ApJ*, 736, 86
- Eilers, A.-C., Davies, F. B., Hennawi, J. F., et al. 2017, *ApJ*, 840, 24
- Eilers, A.-C., Hennawi, J. F., & Davies, F. B. 2018, *ApJ*, 867, 30
- Fan, X., Narayanan, V. K., Lupton, R. H., et al. 2001, *AJ*, 122, 2833
- Fan, X., Strauss, M. A., Becker, R. H., et al. 2006, *AJ*, 132, 117
- Freudling, W., Corbin, M. R., & Korista, K. T. 2003, *ApJL*, 587, L67
- Ge, X., Zhao, B.-X., Bian, W.-H., & Frederick, G. R. 2019, *AJ*, 157, 148
- Grandi, S. A. 1982, *ApJ*, 255, 25
- Gravity Collaboration, Sturm, E., Dexter, J., et al. 2018, *Natur*, 563, 657
- Greene, J. E., Strader, J., & Ho, L. C. 2020, *ARA&A*, in press
- Greggio, L., & Renzini, A. 1983, *A&A*, 118, 217
- Hamann, F., & Ferland, G. 1992, *ApJL*, 391, L53
- Hamann, F., & Ferland, G. 1993, *ApJ*, 418, 11
- Hamann, F., & Ferland, G. 1999, *ARA&A*, 37, 487
- Hamann, F., Korista, K. T., Ferland, G. J., Warner, C., & Baldwin, J. 2002, *ApJ*, 564, 592
- Inayoshi, K., Visbal, E., & Haiman, Z. 2020, *ARA&A*, in press
- Iwamoto, K., Brachwitz, F., Nomoto, K., et al. 1999, *ApJS*, 125, 439
- Iwamuro, F., Kimura, M., Eto, S., et al. 2004, *ApJ*, 614, 69
- Iwamuro, F., Motohara, K., Maihara, T., et al. 2002, *ApJ*, 565, 63
- Izumi, T., Onoue, M., Matsuoka, Y., et al. 2019, *PASJ*, 71, 111
- Izumi, T., Onoue, M., Shirakata, H., et al. 2018, *PASJ*, 70, 36
- Jiang, L., Fan, X., Vestergaard, M., et al. 2007, *AJ*, 134, 1150
- Jiang, L., McGreer, I. D., Fan, X., et al. 2016, *ApJ*, 833, 222
- Juarez, Y., Maiolino, R., Mujica, R., et al. 2009, *A&A*, 494, L25
- Kawara, K., Murayama, T., Taniguchi, Y., & Arimoto, N. 1996, *ApJL*, 470, L85
- Kelson, D. D. 2003, *PASP*, 115, 688
- Kurk, J. D., Walter, F., Fan, X., et al. 2007, *ApJ*, 669, 32
- Maiolino, R., Juarez, Y., Mujica, R., Nagar, N. M., & Oliva, E. 2003, *ApJL*, 596, L155
- Maiolino, R., & Mannucci, F. 2019, *A&ARv*, 27, 3
- Maiz, D., & Mannucci, F. 2012, *PASA*, 29, 447
- Maiz, D., Mannucci, F., & Nelemans, G. 2014, *ARA&A*, 52, 107
- Matsuoka, K., Nagao, T., Maiolino, R., Marconi, A., & Taniguchi, Y. 2009, *A&A*, 503, 721
- Matsuoka, K., Nagao, T., Maiolino, R., Marconi, A., & Taniguchi, Y. 2011a, *A&A*, 532, L10
- Matsuoka, K., Nagao, T., Marconi, A., Maiolino, R., & Taniguchi, Y. 2011b, *A&A*, 527, A100
- Matsuoka, Y., Iwasawa, K., Onoue, M., et al. 2019a, *ApJ*, 883, 183
- Matsuoka, Y., Onoue, M., Kashikawa, N., et al. 2016, *ApJ*, 828, 26
- Matsuoka, Y., Onoue, M., Kashikawa, N., et al. 2019b, *ApJL*, 872, L2
- Matteucci, F., & Greggio, L. 1986, *A&A*, 154, 279
- Mazzucchelli, C., Bañados, E., Venemans, B. P., et al. 2017, *ApJ*, 849, 91
- Meyer, R. A., Bosman, S. E. I., & Ellis, R. S. 2019, *MNRAS*, 487, 3305
- Mortlock, D. J., Warren, S. J., Venemans, B. P., et al. 2011, *Natur*, 474, 616
- Nagao, T., Maiolino, R., & Marconi, A. 2006a, *A&A*, 447, 863
- Nagao, T., Marconi, A., & Maiolino, R. 2006b, *A&A*, 447, 157
- Nomoto, K., Kobayashi, C., & Tominaga, N. 2013, *ARA&A*, 51, 457
- Novak, M., Bañados, E., Decarli, R., et al. 2019, *ApJ*, 881, 63
- Onoue, M., Kashikawa, N., Matsuoka, Y., et al. 2019, *ApJ*, 880, 77
- Planck Collaboration, Adam, R., Aghanim, N., et al. 2016, *A&A*, 596, A108
- Plotkin, R. M., Shemmer, O., Trakhtenbrot, B., et al. 2015, *ApJ*, 805, 123
- Prochaska, J. X., Hennawi, J. F., Westfall, K. B., et al. 2020, pypeit/Pypelit: Release 1.0.0, Zenodo, doi:10.5281/zenodo.3743493
- Reed, S. L., McMahon, R. G., Banerji, M., et al. 2015, *MNRAS*, 454, 3952
- Richards, G. T., Kruczek, N. E., Gallagher, S. C., et al. 2011, *AJ*, 141, 167
- Richards, G. T., Lacy, M., Storrie-Lombardi, L. J., et al. 2006, *ApJS*, 166, 470
- Rodney, S. A., Riess, A. G., Strolger, L.-G., et al. 2014, *AJ*, 148, 13
- Rousselot, P., Lidman, C., Cuby, J. G., Moreels, G., & Monnet, G. 2000, *A&A*, 354, 1134
- Sameshima, H., Yoshii, Y., & Kawara, K. 2017, *ApJ*, 834, 203
- Selsing, J., Fynbo, J. P. U., Christensen, L., & Krogager, J. K. 2016, *A&A*, 585, A87
- Shen, Y. 2013, *BASI*, 41, 61
- Shen, Y., Brandt, W. N., Richards, G. T., et al. 2016, *ApJ*, 831, 7
- Shen, Y., Wu, J., Jiang, L., et al. 2019, *ApJ*, 873, 35
- Shin, J., Nagao, T., Woo, J.-H., & Le, H. A. N. 2019, *ApJ*, 874, 22
- Storchi Bergmann, T., Bica, E., & Pastoriza, M. G. 1990, *MNRAS*, 245, 749
- Tang, J.-J., Goto, T., Ohya, Y., et al. 2019, *MNRAS*, 484, 2575
- Thompson, K. L., Hill, G. J., & Elston, R. 1999, *ApJ*, 515, 487
- Tsuzuki, Y., Kawara, K., Yoshii, Y., et al. 2006, *ApJ*, 650, 57
- van Dokkum, P. G. 2001, *PASP*, 113, 1420
- Vanden Berk, D. E., Richards, G. T., Bauer, A., et al. 2001, *AJ*, 122, 549
- Venemans, B. P., Findlay, J. R., Sutherland, W. J., et al. 2013, *ApJ*, 779, 24



- Venemans, B. P., Neeleman, M., Walter, F., et al. 2019, [ApJL](#), 874, L30
- Venemans, B. P., Walter, F., Decarli, R., et al. 2017a, [ApJ](#), 837, 146
- Venemans, B. P., Walter, F., Decarli, R., et al. 2017b, [ApJL](#), 851, L8
- Venemans, B. P., Walter, F., Zschaechner, L., et al. 2016, [ApJ](#), 816, 37
- Verner, E. M., Verner, D. A., Korista, K. T., et al. 1999, [ApJS](#), 120, 101
- Vestergaard, M., & Osmer, P. S. 2009, [ApJ](#), 699, 800
- Vestergaard, M., & Wilkes, B. J. 2001, [ApJS](#), 134, 1
- Vietri, G., Piconcelli, E., Bischetti, M., et al. 2018, [A&A](#), 617, A81
- Wang, F., Yang, J., Fan, X., et al. 2018, [ApJL](#), 869, L9
- Wang, R., Wagg, J., Carilli, C. L., et al. 2013, [ApJ](#), 773, 44
- Wang, R., Wu, X.-B., Neri, R., et al. 2016, [ApJ](#), 830, 53
- Willott, C. J., Delorme, P., Reyl , C., et al. 2010, [AJ](#), 139, 906
- Woo, J.-H., Le, H. A. N., Karouzos, M., et al. 2018, [ApJ](#), 859, 138
- Wu, X.-B., Wang, F., Fan, X., et al. 2015, [Natur](#), 518, 512
- Xu, F., Bian, F., Shen, Y., et al. 2018, [MNRAS](#), 480, 345
- Yang, J., Wang, F., Fan, X., et al. 2019, [AJ](#), 157, 236
- York, D. G., Adelman, J., Anderson, J. E., et al. 2000, [AJ](#), 120, 1579
- Yoshii, Y., Tsujimoto, T., & Kawara, K. 1998, [ApJL](#), 507, L113